

The ALPINE-CRISTAL-JWST Survey: Gas-phase abundance gradients of main sequence star-forming galaxies and their kinematics at $4 < z < 6$

Lilian L. Lee^{1,*}, N. M. Förster Schreiber¹, S. Fujimoto^{2,3}, A. L. Faisst⁴, R. Herrera-Camus^{5,6}, R. Genzel^{1,7}, L. J. Tacconi¹, D. Lutz¹, A. Renzini⁸, R. Sanders⁹, E. Wisnioski¹⁰, S. Wuyts¹¹, E. Parlanti^{12,1}, G. Jones^{13,14}, H. Übler¹, D. Liu¹⁵, J. Chen¹, R. I. Davies¹, G. Tozzi¹, A. Burkert^{16,1}, S. H. Price¹⁷, M. Aravena^{18,19}, M. Boquien²⁰, M. Béthermin²¹, E. da Cunha²², R. L. Davies²³, I. De Looze²⁴, M. Dessauges-Zavadsky²⁵, A. Ferrara¹², D. B. Fisher²⁶, S. Gillman^{27,28}, M. Ginolfi²⁹, E. Ibar^{30,31}, A. M. Koekemoer³², J. Molina^{30,31}, T. Naab³³, M. Relaño^{34,35}, D. A. Riechers³⁶, D. B. Sanders³⁷, J. S. Spilker³⁸, L. Vallini³⁹, G. Zamorani³⁹, A. Nanni^{40,41}, P. Dam⁴², T. Diaz-Santos^{43,44}, D. Gómez-Espinoza^{30,31}, A. Hadi⁴⁵, R. Ikeda^{46,47}, A. Posses³⁸, M. Romano^{48,49}, A. Sternberg^{50,51}, V. Villanueva⁵, and W. Wang⁴

(Affiliations can be found after the references)

Received XXX; accepted YYY

ABSTRACT

We present gas-phase radial metallicity profiles for 20 main-sequence galaxies at $4 < z < 6$, primarily based on JWST NIRSpec IFU observations obtained as part of the JWST-ALPINE-CRISTAL programme. Our study aims to connect the metallicity gradients of these galaxies with their kinematic properties from [C II] $158\mu\text{m}$ ALMA observations. We map the radial profiles of oxygen abundance using the strong-line method leveraging the rich set of rest-frame optical emission lines. Linear fits to the annular-binned radial profiles show that, on average, the metallicity gradients are slightly positive with a median of $+0.039 \pm 0.010 \text{ dex kpc}^{-1}$. There are no substantial systematic offsets in gradients when using different line diagnostics. However, only three galaxies show a gradient $> 0.05 \text{ dex kpc}^{-1}$ at 1σ , and none have a significant negative gradient. We investigate the correlation between the metallicity gradients and the intrinsic gas velocity dispersion σ_0 , as well as the ratio V_{rot}/σ_0 of the disks. Combining our sample with mass-matched literature samples at $3 \lesssim z \lesssim 7$, we find a negative shallow correlation between V_{rot}/σ_0 and the metallicity gradients, but no strong relationships with σ_0 . As V_{rot}/σ_0 increases towards later cosmic times, the observed negative trend with V_{rot}/σ_0 is consistent with the overall cosmic evolution of metallicity gradients from high to low redshifts. This suggests that disk maturity plays a crucial role in shaping the radial metallicity gradients. We do not find the metallicity gradients of disk galaxies significantly different from non-disk galaxies, which could be attributed to the frequent accretion events that took place in these gas-rich systems. Additionally, we find no strong dependence of metallicity gradients on stellar mass and only a marginal positive dependence on specific star-formation rate. Our study extends the efforts to connect the internal kinematics of galaxies with their gas-phase chemical enrichment at kpc scales from cosmic noon to $z > 4$.

Key words. galaxies: high-redshift — galaxies: abundances — galaxies: kinematics and dynamics — galaxies: galaxy evolution

1. Introduction

The distribution of heavy elements (metals) at high redshifts ($z \gtrsim 1$) places important constraints on the effects of gas flows in the early phase of disk growth. The radial gradient of oxygen abundance (metallicity gradient henceforth), or of other α elements, in the gas phase is commonly used as a sensitive probe of baryonic assembly, and the complex gas flows driven by both galactic feedback and tidal interactions that can transport the stellar nucleosynthesis yields from where they are produced. In the local Universe, observations from various large surveys indicate a typical negative gas-phase metallicity gradient of oxygen ranging from ~ -0.05 to 0 dex kpc^{-1} (e.g. Zaritsky et al. 1994; Sánchez et al. 2014; Ho et al. 2015; Grasha et al. 2022), indicating a chemically richer central region compared to the outskirts. Similarly for the Milky Way, typical radial metallicity gradients inferred from different tracers range from -0.06 to $-0.01 \text{ dex kpc}^{-1}$ (Maiolino & Mannucci 2019, and references therein). The observed negative metallicity gradient in the local

Universe could arise from an inside-out growth scenario, where the inner disk forms stars first from the high density of gas and has more time to enrich the interstellar medium (ISM) than the outer regions (e.g. Matteucci & Francois 1989).

Metallicity measurements of galaxies at cosmic noon ($z \sim 1-3$), obtained with sensitive Integral Field Units (IFUs) mounted on 8–10 m class ground-based telescopes, have revealed a wide range of metallicity gradients, with both negative, positive, and flat gradients observed (Cresci et al. 2010; Yuan et al. 2011; Queyrel et al. 2012; Swinbank et al. 2012b; Jones et al. 2013; Stott et al. 2014; Troncoso et al. 2014; Leethochawalit et al. 2016; Wuyts et al. 2016a; Wang et al. 2017, 2022; Carton et al. 2018; Förster Schreiber et al. 2018; Curti et al. 2020a). Some studies suggest that more massive galaxies tend to have steeper metallicity gradients, while galaxies with higher specific star formation rates (sSFRs) tend to have flatter gradients (e.g. Gillman et al. 2021; Cheng et al. 2024). The majority of $z \lesssim 3$ results are consistent with flat within errors or only moderately negative.

In the case of the Milky Way, its metallicity gradient (of oxygen) has evolved from $\sim -0.01 \text{ dex kpc}^{-1}$ at $z = 1$ to the current

* Corresponding author; lilian@mpe.mpg.de; mail@lilianlylee.com

steepness of $\sim -0.04 \text{ dex kpc}^{-1}$ based on e.g. planetary nebulae that probe longer look-back times and chemical evolution models (Chiappini et al. 2001; Stanghellini et al. 2014; Mollá et al. 2019). Therefore, based on observations, one expects metallicity gradients to become increasingly negative with cosmic time, eventually matching the steeper gradients seen in nearby disks. This evolutionary trend is reproduced in only a subset of simulations (e.g. MaGICC, Gibson et al. 2013). Most simulations, however, predict the opposite behaviour, namely that gradients start steeper at high redshift and subsequently flatten (Taylor & Kobayashi 2017; Acharyya et al. 2025; Garcia et al. 2025), while others find very little evolution between $z \lesssim 3$ and the present epoch (Ma et al. 2017; Hemler et al. 2021; Tissera et al. 2022; Sun et al. 2025). The difference in behaviour is largely because of the influence of feedback, where models or simulations with strong feedback lead to flatter gradients at higher redshifts when feedback and outflows were more important.

The advent of the *James Webb* Space Telescope (JWST) has enabled access to multiple rest-frame strong optical lines at $z > 4$. Recent JWST-based metallicity measurements suggest flat to positive gradients for a large fraction of galaxies at $z > 6$, albeit based on a heterogeneous sample (Arribas et al. 2024; Venturi et al. 2024; Barišić et al. 2025; Li et al. 2025b; Ju et al. 2025, see also Birkin et al. 2023). However, there have been no systematic studies of metallicity gradients at $4 < z < 6$ to date.

Several internal secular processes can contribute to the flattening or even inversion of the gas-phase metallicity gradients in disk galaxies, or even prevent the formation of gradients altogether. Radial flows of gas and migration of young massive stars, for instance, can dilute the central regions and flatten the metallicity gradients (Spitoni & Matteucci 2011; Mott et al. 2013; Spitoni et al. 2015). Additionally, strong feedback in the form of galactic outflows can redistribute metals produced by the central starburst region towards the external regions of galactic disks, potentially inverting the gradient to become positive if the outflows have a strong metal-loading (Tissera et al. 2022). The presence of a bar may also play a role in flattening the abundance gradient, likely due to the non-circular motions induced in the gas (e.g. Alloin et al. 1981; Zaritsky et al. 1994) with its impact correlating with bar strength (Martin & Roy 1994, but see Sánchez-Menguiano et al. 2018 and Wisz et al. 2025 for a contrasting view).

Positive gradients could also result from external stochastic processes such as galaxy interactions (Rupke et al. 2010a; Taylor & Kobayashi 2017) or the dilution of metallicity in the central regions by cold flows of pristine gas from the intergalactic medium (Dekel et al. 2009). The complex interplay between these various mechanisms could contribute to the observed diversity of metallicity gradients in galaxies (Sharda et al. 2021a).

Nevertheless, simulation work on metallicity gradients have largely been focussed at $z \lesssim 3$, with only a handful of studies covering earlier cosmic epochs (e.g. Garcia et al. 2025; Ibrahim & Kobayashi 2025). Most simulations predict strong negative metallicity gradients at early cosmic times, likely due to their similar treatments of relatively smooth stellar feedback allowing for sustained inside-out growth and weak sub-grid metal diffusion (Hemler et al. 2021; Tissera et al. 2022; Sun et al. 2025, see discussion in Garcia et al. 2025).

From a dynamical perspective, kinematics and metals distribution are tightly connected. At low-redshift and up to $z \sim 1-3$, an emerging trend suggests that more turbulent galaxies, characterised by their low rotational support relative to velocity disper-

sion, tend to have flatter metallicity gradients (e.g. Queyrel et al. 2012; Jones et al. 2013; Leethochawalit et al. 2016; Lyu et al. 2025), a tendency also seen in simulations (Ma et al. 2017; Hemler et al. 2021) and reproduced well with analytical models with efficient metal mixing (e.g. Sharda et al. 2021b). In general, the flat gradient can be attributed to the unstable internal dynamics of turbulent disks, making them more susceptible to disturbances caused by strong feedback-driven gas flows, in addition to mixing from advection and accretion. As a result, large-scale metal redistribution over several kiloparsecs (kpc) within the galaxy can occur, leading to the flat to positive gradients observed.

At cosmic noon and up to $z \sim 4$, there is also growing evidence suggesting the prevalence of non-circular motion and radial gas flows in gas-rich disk galaxies, characterised by velocities of the order of few tens of km s^{-1} , which could efficiently transport gas inwards (e.g. Price et al. 2021; Genzel et al. 2023; Übler et al. 2024; Tsukui et al. 2024; Huang et al. 2025; Pastras et al. 2025). If these secular mixing processes occur on a timescale comparable to that of metal production by stars, the ISM could remain well mixed from the outset, and stayed such way until the disk settles into a dynamically cold and thin disk, at which point the classical inside-out formation scenario may dominate, leading to a negative metallicity gradient.

While measurements of metallicity gradients in galactic disks at $z > 4$ remain scarce due to rest-frame optical lines being shifted out of the atmospheric window, kinematics studies are benefitted from sub-mm interferometers such as ALMA and NOEMA, with the bright [C II] line emission as a commonly used tracer. The [C II] line is a primary radiative line coolant of the cold ISM, associated with photo-dissociation region (PDR) and H II regions (e.g. Wolfire et al. 2003; Vallini et al. 2015; Clark et al. 2019). The high spectral and spatial resolution of these facilities have allowed for high-resolution resolved kinematics at scales of $\sim 1 \text{ kpc}$ (e.g. Tsukui & Iguchi 2021; Rizzo et al. 2021; Roman-Oliveira et al. 2023; Rowland et al. 2024; Lee et al. 2025a).

We here exploit the synergy between ALMA and JWST to investigate the connection between the kinematic nature and metallicity gradients of star-forming galaxies (SFGs) at $4 < z < 6$, a previously under-explored area. Our analysis combines ALMA-CRISTAL survey data (Herrera-Camus et al. 2025), which provides high-resolution kinematic information via the [C II] line emission, with JWST NIRSpec IFU data from primarily the JWST-ALPINE-CRISTAL survey (Faisst et al. 2026), which enables the measurement of chemical abundance gradients using strong rest-optical nebular lines that are commonly used at lower redshift.

Our sample consists of a homogeneously selected set of main-sequence (MS) SFGs representative of the galaxy population at $4 < z < 6$. Building on the kinematic analysis presented in Lee et al. (2025a), we aim to explore the relationship between internal dynamics and chemical abundance distribution in these galaxies, and investigate potential differences between disk and non-disk galaxies classified in Lee et al. (2025a). The differences between the kinematic classifications using the ALPINE and CRISTAL data are discussed in more detail by Lee et al. (2025a).

Separate work by Faisst et al. (2025) will present a more detailed analysis of the integrated metallicity and mass-metallicity relation. Fujimoto et al. (2025) will discuss the cosmic evolution of metallicity gradients, and in conjunction with F. Lopez et al. (in prep.), they will present the metallicity maps for the full JWST-ALPINE-CRISTAL sample. This work builds upon

the analysis of Fujimoto et al. (2025) by incorporating a broader range of strong line diagnostics available from the data. Additionally, we investigate the impact of different diagnostics and beam smearing on the resulting metallicity gradients, thereby complementing the analysis of Fujimoto et al. (2025).

This work is structured as follows. In Sect. 2, we describe the sample selection and data reduction process. Sect. 3 presents the method of emission line fitting, followed by Sect. 4 that describes the methods used to infer metallicity and examines the systematic effects of different strong-line diagnostics on the inferred gradients. Sect. 5 explores the relationship between the measured metallicity gradients and their kinematic nature, as well as other physical properties of the samples. Sect. 6 investigates the impacts of beam smearing on the inferred metallicity gradients. Finally, Sect. 7 summarises the key findings.

Throughout, we adopt a flat Λ CDM cosmology with $H_0 = 70 \text{ km s}^{-1} \text{ Mpc}^{-1}$, and $\Omega_m = 0.3$. Solar metallicity is taken to be $12 + \log(\text{O}/\text{H}) = 8.69$ (Asplund et al. 2009). Where relevant, Chabrier (2003) initial mass function (IMF) is used. Physical size is always reported in physical kiloparsecs (kpc), but we use kpc henceforth for brevity.

2. Samples

In this study, we investigate the abundance distribution of the sample presented in Lee et al. (2025a), which examines the kinematic properties of 32 galaxies at $4 < z < 6$ using [C II] emission, as part of the ALMA-CRISTAL survey (Herrera-Camus et al. 2025) and samples supplemented from the ALMA archive. The NIRSpec/IFU data used for metallicity measurements are drawn from the JWST-ALPINE-CRISTAL survey (PID: 3045, PI: A. Faisst), a GO programme (PID: 4265, PI: J. Gonzalez Lopez) and the Galaxy Assembly with NIRSpec Integral Field Spectroscopy (GA-NIFS) Guaranteed Time Observations (GTO) programme (PID: 1217, PI: N. Luetzendorf). The NIRSpec data from JWST-ALPINE-CRISTAL survey additionally covers vc_5110377875 (VC-7875 henceforth), for which the kinematics results are presented in Fujimoto et al. (2020) and Jones et al. (2021). The key properties of our sample are listed in Table 1.

For a detailed description of the samples, we refer the reader to the survey papers: Herrera-Camus et al. (2025) for the original ALMA-CRISTAL sample and Faisst et al. (2026) for the NIRSpec/IFU data and data reduction (Fujimoto et al. 2025).

In brief, ALMA-CRISTAL (Herrera-Camus et al. 2025) is a high-resolution follow-up of a subset of galaxies from the ALMA-ALPINE survey (B  thermin et al. 2020; Le F  vre et al. 2020; Faisst et al. 2020), with stellar masses $\log(M_\star/M_\odot) \geq 9.5$ and sSFRs within a factor of 3 of the main sequence, with higher angular resolution, resolving the galaxies at $\sim 1 \text{ kpc}$ scale.¹ Both programmes carried out ALMA observations in Band 7, targeting [C II] $158 \mu\text{m}$ and the dust continuum emission of MS SFGs at $4 < z < 6$. The JWST-ALPINE-CRISTAL survey is a NIRSpec IFU follow-up of 18 galaxies from the two ALMA large programmes.

The NIRSpec/IFU data cover a wavelength range of 1.66 to $5.10 \mu\text{m}$ (rest-frame 0.28–0.85 μm at $z = 5$) at a medium spectral resolution of $R \sim 1000$ ($\approx 125 \text{ km s}^{-1}$ at $3 \mu\text{m}$) with two gratings: G235M and G395M.

¹ The ALMA data of VC-7875 and CRISTAL-24 (DEIMOS_COSMOS_873756) also come from two other ALMA observations (ALMA project 2019.1.00226.S, 2022.1.01118.S, PIs: E. Ibar, M. B  thermin).

Since the JWST-ALPINE-CRISTAL sample does not include all galaxies in the kinematics sample presented in Lee et al. (2025a), we supplement our analysis by incorporating NIRSpec/IFU data for CRISTAL-01, 20, and 22a from two separate programmes. Specifically, we utilise data from a GO programme (PID: 4265, PI: J. Gonzalez Lopez, Solimano et al. 2025) for CRISTAL-01, and from the GA-NIFS survey for CRISTAL-20 and 22a. The GO programme employed a nine-point (‘SMALL’) dither pattern, while the GA-NIFS GTO programme used an eight-point (‘MEDIUM’) dither pattern. Both datasets were obtained at high spectral resolution using the G395H/F290LP configuration, which provides a spectral resolution of $R \sim 2700$. For CRISTAL-20 and 22a, we adopt the published metallicity maps presented in Parlanti et al. (2025a) and Jones et al. (2025), respectively, which have a pixel scale of $0''.05 \text{ pix}^{-1}$. We examine their different adopted calibrations, and any differences they may introduce to the metallicity gradients in Sect. 4.

The important rest-frame optical emission lines for inferring metallicity, listed in order of increasing wavelength, are: [O II] $\lambda\lambda 3726, 29$, [Ne III] $\lambda 3869$, H β , [O III] $\lambda\lambda 4959, 5007$, [N II] $\lambda\lambda 6548, 6583$, H α , and [S II] $\lambda\lambda 6716, 6731$. Higher Balmer transition lines up to H ϵ are also detected in some cases (Fujimoto et al. 2025; Faisst et al. 2026). The auroral line [O III] $\lambda 4363$ is also detected in five galaxies, and for these cases, the non- T_e -based metallicities are in good agreement with the T_e -based metallicities, albeit with larger uncertainties (Faisst et al. 2025).

Six objects in our sample were classified as candidate Type-1 AGNs by Ren et al. (2025) (see Table 1) due to the tentative presence of broad H α emission. We retain these objects in the sample because their [N II]/H α ratios are low ($f_{\text{[N II]}}/f_{\text{H}\alpha} \lesssim 0.1$) and they lie very close to the star-forming locus in the classical Baldwin, Phillips, & Terlevich (1981, BPT) diagrams. The same holds when using higher-ionisation diagnostics: the He II $\lambda 4686$ -based criterion of Shirazi & Brinchmann (2012) and the [O III] $\lambda 4363$ /H γ -based demarcation of Mazzolari et al. (2024); they would also fall well below the revised AGN boundary of Scholtz et al. (2025). The He II and [O III] $\lambda 4363$ lines are, however, too faint to construct spatially resolved maps that would separate AGN- and star-formation-dominated regions, leaving the less suitable [N II]-based BPT diagram as the only feasible option (as in Ren et al. 2025). Hence, although an AGN contribution cannot be entirely ruled out, the available diagnostics provide no compelling evidence for a strong one; any putative AGN should therefore be weak, and contamination from AGN-driven shocks or excess hard ionising radiation is expected to be minor.

There is nonetheless one galaxy, CRISTAL-24, that has a very high [N II]/H α (Ren et al. 2025) hinting at strong AGN activity or the presence of shocks (e.g. Dopita & Sutherland 1995). We therefore excluded this galaxy from our analysis. The stacking of [C II] data indicates that the sample as a whole exhibits weak outflow signatures (Birkin et al. 2025), and for the majority of the sample, outflows are expected to have a negligible impact on the line fluxes. CRISTAL-17 (DEIMOS_COSMOS_742174) is also not included in this work since it is too faint in the ALMA data for kinematic classification and modelling in Lee et al. (2025a). The metallicity gradients of CRISTAL-17 and 24 are investigated in Fujimoto et al. (2025). The final sample size of our study is 20.

Table 1: Physical properties of the 20 galaxies in the sample.

CRISTAL ID	Full name	$z_{[\text{C II}]}$	R.A. ($^{\circ}$)	Decl. ($^{\circ}$)	$\log(M_{\star}/M_{\odot})^a$ (dex)	$\log[\text{SFR}/(M_{\odot} \text{ yr}^{-1})]^a$ (dex)	Class. ^b
01	DC_842313	4.554	150.2271	2.5762	10.65	2.31	Non-Disk
02 [†]	DC_848185, HZ6, LBG-1	5.294	150.0896	2.5864	10.30	2.25	Disk
03 [†]	DC_536534, HZ1	5.689	149.9719	2.1182	10.40	1.79	Best-Disk ^c
04a	vc_5100822662	4.520	149.7413	2.0809	10.15	1.89	Non-Disk
05 [†]	DC_683613, HZ3	5.541	150.0393	2.3372	10.16	1.83	Disk
06a	vc_5100541407	4.562	150.2538	1.8094	10.09	1.62	Disk
06b	...	4.562	150.2542	1.8097	9.19	1.07	Non-Disk
07a [†]	DC_873321, HZ8	5.154	150.0169	2.6266	10.00	1.89	Disk
07b	...	5.154	150.0166	2.6268	Non-Disk
09 [†]	DC_519281	5.575	149.7537	2.0910	9.84	1.51	Disk ^c
10a-E [†]	DC_417567, HZ2	5.671	150.5172	1.9290	9.99	1.86	Disk
11	DC_630594	4.439	150.1358	2.2579	9.68	1.57	Best Disk ^c
13	vc_5100994794	4.579	150.1715	2.2873	9.65	1.51	Non-Disk
14	DC_709575	4.411	149.9461	2.3758	9.53	1.45	Non-Disk ^d
15	vc_5101244930	4.580	150.1986	2.3006	9.69	1.44	Best Disk
19	DC_494763	5.233	150.0213	2.0534	9.51	1.45	Best Disk ^c
20	DC_494057, HZ4	5.545	149.6188	2.0518	10.11	1.82	Best Disk ^e
22a	HZ10-E	5.653	150.2471	1.5554	10.35	2.13	Disk
25	vc_5101218326	4.573	150.3021	2.3146	10.90	2.75	Non-Disk
VC-7875	vc_5110377875	4.551	150.3848	2.4084	10.17	2.00	Disk ^f

Notes. ^(a) Derived from SED modellings in [Mitsuhashi et al. \(2024\)](#) and [Li et al. \(2024\)](#). The typical uncertainty for $\log(M_{\star})$ and $\log(\text{SFR})$ are about 0.3 dex. ^(b) Classified in [Lee et al. \(2025a\)](#). ^(c) Classified as rotating disks also in D. Gomez-Espinoza et al. (in prep.) with the $\text{H}\alpha$ data. ^(d) Classified as compact in D. Gomez-Espinoza et al. (in prep.). ^(e) Candidate Type-1 AGNs identified in [Ren et al. \(2025\)](#) based on the tentative detection of $\text{H}\alpha$ broad component. ^(f) See [Parlanti et al. 2025a](#) for a contrasting view. ^(g) Classified as ‘Rotator’ in [Jones et al. \(2021\)](#) but with signatures of interaction with an extended halo or an extended outflow ([Fujimoto et al. 2020](#)), so it will fall closest to the ‘Disk’ classification in [Lee et al. \(2025a\)](#).

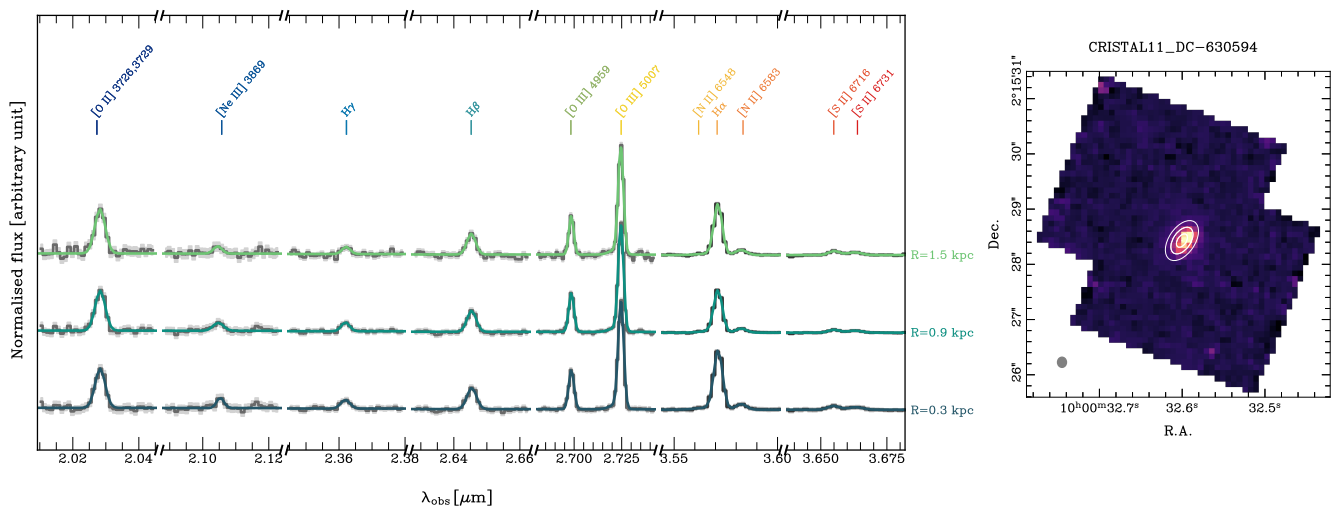


Fig. 1: Example spectral fit of CRISTAL-11 ($z = 4.439$) for each annulus (*left*). The fitting procedure of the spectra is described in Sect. 3. The radius of the corresponding annulus is indicated in physical units on the right. The lines used for inferring metallicity in Sect. 4 are annotated at the top. The shape of the annuli are shown in the *right* panel, overlaid on the line flux map of $\text{H}\alpha$. The PSF after PSF homogenisation is shown at the bottom left.

3. Emission line measurements

To avoid introducing artificial metallicity gradients caused by variations in angular resolution as a function of wavelength, we homogenise the point spread function (PSF) of all channels to the size of the PSF at the wavelength of the reddest line used in our metallicity diagnostics (see Sect. 4). This line is chosen as either $[\text{S II}] \lambda 6731$ or $[\text{N II}] \lambda 6583$, depending on whether $[\text{S II}]$ is detected with sufficient S/N. Since no stars are detected in our

data cubes, we characterise the PSF using a data cube from another GO program (PID: 2957, PIs: H. Übler and R. Maiolino). In each channel, we fit a 2D Gaussian to the star to determine the orientation and size of the PSF both across and along the slicer. We observe that the PSF is more elongated in the direction along the IFU slicer, consistent with [D’Eugenio et al. \(2024\)](#). The minor and major axes of the PSF range from $[0.16, 0.18]''$ and $[0.19, 0.20]''$, respectively, equivalent to 1–1.3 kpc at $z = 5$.

We follow the same background subtraction method as in Fujimoto et al. (2025). After subtraction of the background from the datacube, and PSF homogenisation with the PSF models constructed above, by convolving each image with a kernel whose σ equals the quadrature difference between its native PSF and the chosen target PSF, we sum spectra from spaxels located within concentric elliptical annuli.

The annuli had a width equal to one PSF HWHM (half-width at half-maximum, taken as the geometric mean of the along- and across-slicer directions), with typical width of $\lesssim 0''.2$, ≈ 0.6 kpc at $z=5$. The galactocentric radius assigned to every spaxel is taken to be $(a_{\text{in}} + a_{\text{out}})/2$, where a_{in} and a_{out} are the inner and outer semi-major-axis lengths of the elliptical annulus that contains the spaxel. Because an intrinsically thin disk is not compressed along its major axis, this definition already gives the true (de-projected) radius for such systems. However, for our galaxies that are likely not well described by thin disks, the same quantity is only a projected radius, with de-projection requiring an assumption on the intrinsic disk thickness. These geometric ambiguities introduce an additional systematic uncertainty when our gradients are compared to literature measurements that adopt different assumptions about galaxy geometry, as will be discussed in Sect. 5.

We adjust the number of rings based on the outermost radius set by the S/N of the integrated line maps of [O III] $\lambda 5007$ or $H\alpha$. However, when calculating line flux ratios, we consider the S/N of the individual lines involved in the extracted spectra, the outermost radii for each line diagnostic therefore vary. At this stage we do not apply any pixel-by-pixel rejection. The spectra are extracted using all pixels in an annulus, and the selection relies solely on the azimuthally integrated S/N. Rejection of pixels that have low fluxes to give robust line ratios is introduced later, in Sect. 5.3, where we investigate azimuthal variations across radii. The apparent centre, axial ratio and position angle of the galaxy are derived from the emission line maps of the brightest line, either [O III] $\lambda 5007$ or $H\alpha$, by fitting a 2D Gaussian profile. In most cases, the centres coincide with those of the [C II] moment-0 maps to within one NIRSpect pixel ($0''.1$), although the ALMA [C II] data have a spatial resolution that is 2–4 \times worse than that of NIRSpect. The error spectrum is calculated as the root-mean square (RMS) error using a moving window of 160 channels, with emission lines and any spurious noise spikes masked out.

We correct for dust reddening by comparing the observed Balmer line ratios to the theoretical values on an annulus-to-annulus basis. We assume the theoretical $H\alpha/H\beta$ ratio equal to 2.86 as expected for case-B recombination (i.e., ionising photons are absorbed as soon as they are emitted) and an electron temperature of $T_e \sim 10^4$ K (Osterbrock & Ferland 2006, Table 4.2). We then assume the nebular extinction that follows the Calzetti et al. (2000) curve. For CRISTAL-06a and 25, the $H\beta$ emission is too weak in the individual annuli, we then apply the correction using a global A_V which is inferred from the spectrum integrated over a larger aperture with size covering the entire galaxy. For other galaxies, the mean offset between the radially resolved and integrated A_V is 0.05 with a standard deviation of 0.34, so while individual annuli can deviate, the typical variation in A_V is small compared to the uncertainties, and would not significantly change the measured gradients of CRISTAL-06a and 25.

CRISTAL-06b has no $H\beta$ detection even in the integrated spectrum, so we adopt only diagnostics that are close in wavelength for inferring metallicity. For some galaxies, higher transi-

tion Balmer lines $H\gamma$ and $H\delta$ are also detected at lower S/N.² They tend to give more uncertain A_V than that inferred from $H\alpha/H\beta$. We therefore adopt the A_V from $H\alpha/H\beta$ only. We do not correct for Galactic extinction explicitly, since for our sources, the foreground Galactic $A_V \lesssim 0.4$ mag (Schlafly & Finkbeiner 2011), and becomes negligible at IR wavelengths following Fitzpatrick & Massa (2007) extinction curve.

To extract the flux for each emission line that will be used in Sect. 4, we use CapFit (Cappellari 2023) to fit a single Gaussian profile to each detected line. We included an underlying first-order polynomial to model the baseline. If present in the spectra, we tie the line ratios of [O III] and [N II] doublets to the theoretical values of 2.98 and 3.071 (Storey & Zeippen 2000), respectively. All emission lines within the same annulus are fixed to the same redshift, but their line centroids are allowed to vary within two channels ($0.002 \mu\text{m}$ or $\approx 160\text{--}300 \text{ km s}^{-1}$ at the wavelengths of interest) from the theoretical wavelength position. This margin accommodates bulk gas motions that can induce velocity shifts of at most $\sim 150 \text{ km s}^{-1}$, as observed for [C II] (see Table 2 of Lee et al. 2025a), as well as the wavelength-dependent line spread function (LSF) across the cube.

Their (observed) line widths are tied to the same value but can vary within five channels as a whole. For five galaxies that are classified as candidate Type-1 AGNs in Ren et al. (2025) (see Table 1), we additionally include a broad Gaussian component to model the emission lines, which otherwise would result in residuals around the narrow component. However, except for the stronger lines such as [O III] $\lambda 5007$, $H\alpha$, and in some cases $H\beta$, the broad component flux converges to zero for other lines, suggesting the S/N for these fainter lines is insufficient to recover the broad component. In cases where the broad component is non-zero, it contributes a relatively small fraction of the total line flux, ranging from a few to $< 20\%$. For our subsequent analysis, we only consider the flux from the narrow component. We find that the gradients are consistent with those obtained when using a single-component fit, only the normalisation differs. This agreement is expected, given that the broad component contributes only a minor fraction of the total line flux. An example best-fit is shown in Fig. 1.

4. Strong line metallicity indicators and metallicity gradients

In this section, we leverage the rich set of lines observed, giving access to multiple strong line diagnostics. As discussed below, different diagnostics have different strengths and combining them would give a tightened constraint on the metallicity. Building on the work of Fujimoto et al. (2025), who presented metallicity gradients inferred from two diagnostics, we expand our analysis to include a broader range of strong line diagnostics available from the data. We assess the impact of different diagnostics on the resulting metallicity gradients, complementing the analysis of Fujimoto et al. (2025).

We derive the gas-phase metallicity by jointly analysing the measured emission line ratios using the empirical calibrations summarised in Table 2. The diagnostic line ratios often involve collisionally-excited lines from either singly and/or doubly ionised oxygen (O^+ and O^{2+}), or singly ionised nitrogen and sulphur (N^+ and S^+), each measured relative to hydrogen recombination lines ($H\alpha$ and $H\beta$ in our case), except for O32

² $H\epsilon$ is detected in some cases; however, due to its blending with [Ne III] $\lambda 3967$, we refrain from using it to infer A_V .

or Ne3O2. The strengths and limitations of each line diagnostic are summarised in Table 1 of [Maiolino & Mannucci \(2019\)](#) (see also [Kewley et al. 2019](#)). In brief, some diagnostics—such as R3—are double-valued with respect to metallicity and thus require auxiliary diagnostics such as O32 and N2 to resolve this degeneracy. Because nitrogen is not an α -element and, at the metallicities relevant to our sample, is produced mainly as a secondary element, nitrogen-line indices probe the oxygen abundance only indirectly through the N/O–O/H correlation. This makes them more sensitive to variations in chemical evolution history than oxygen-based indices. On the other hand, indices such as N2 increase monotonically with O/H, so they do not suffer from the degeneracy that affects R3 and similar oxygen-line diagnostics. Therefore, since some diagnostics are more sensitive to the ionisation parameter, reddening corrections, and nitrogen enrichment than others, we can better marginalise over different systematic effects by combining the various diagnostics. We are aware, however, that the uncertainty estimates from such a Bayesian approach may not be statistically meaningful, since the line ratios are not independent of each other. As discussed later in this section and Appendix B, to estimate uncertainties in an alternative way, we compute the metallicity gradients independently using each diagnostic and calculate the standard deviation of these gradients.

We utilise the empirical relations from [Sanders et al. \(2025\)](#) that are calibrated based on a sample of ~ 140 SFGs at $z \sim 3\text{--}10$ drawn from the AURORA survey (PID: 1914, PIs: A. Shapley and R. Sanders, [Shapley et al. 2025](#)) and the literature, covering the widest range in metallicity where multiple auroral lines are available (e.g. [O III] $\lambda 4363$). It leverages the latter to infer metallicities via the direct electron-temperature (T_e) method, in which elemental abundances are derived from the exponential dependence of line emissivity on T_e measured through highly temperature-sensitive auroral lines. The metallicity range where each diagnostic can be reliably applied is listed in Table 2. Unfortunately, neither [O III] $\lambda 4363$ nor H γ is detected in every annulus of every galaxy, and even the integrated spectra lack robust [O III] $\lambda 4363$ measurements for a number of sources (see [Faisst et al. \(2026\)](#), Table A4, and [Faisst et al. \(2025\)](#), Table 1, for direct- T_e global metallicity, which is only possible for five sources, with an average uncertainty of ≈ 0.3 dex).

In an absolute sense, different calibrations can introduce systematics of up to 0.7 dex ([Kewley & Ellison 2008](#)) in absolute metallicity measurements, due to variations between empirical and theoretical methods, sample selections, and line tracers. However, these uncertainties are less problematic when measuring metallicity gradients, because gradients rely on relative (differential) abundances rather than absolute values, and the relative systematics are typically within ~ 0.15 dex. A more recent study by [Li et al. \(2025a\)](#) (their Fig. 16) found < 0.1 dex scatter around equality when using different strong-line calibrations (e.g. [Maiolino et al. 2008](#); [Curti et al. 2020b](#); [Nakajima et al. 2022](#); [Sanders et al. 2024](#)), which is within their measurement uncertainty; there are no obvious systematic offsets between different calibrations. We verify that the metallicity gradients derived with the calibrations of [Bian et al. \(2018\)](#)³ We also inves-

³ S2 and O2 are not included. and [Nakajima et al. \(2022\)](#)⁴ are in general consistent with those obtained using the [Sanders et al. \(2025\)](#) calibration, differing on average by only -0.01 dex kpc^{-1} and -0.02 dex kpc^{-1} , respectively. In no case did the sign flip when an alternative calibration was applied. Both [Bian et al. \(2018\)](#) and [Nakajima et al. \(2022\)](#), however, are based on local-Universe analogues of high-redshift galaxies. Now that JWST increasingly provides direct auroral-line measurements in high- z galaxies, calibrations anchored to

Table 2: Line diagnostics and the calibrations used.

Indicators	Emission line ratio	Z Range ^a
N2 [†]	[N II] $\lambda 6583/\text{H}\alpha$	[7.8, 8.6]
R3 [†]	[O III] $\lambda 5007/\text{H}\beta$	[7.3, 8.6]
Ne3O2 [†]	[Ne III] $\lambda 3869/([\text{O II}] \lambda \lambda 3726, 29)$	[7.4, 8.6]
O32	[O III] $\lambda 5007/([\text{O II}] \lambda \lambda 3726, 29)$	[7.3, 8.6]
O2	[O II] $\lambda \lambda 3726, 29/\text{H}\beta$	[7.3, 8.6]
S2	[S II] $\lambda \lambda 6716, 33/\text{H}\alpha$	[7.9, 8.6]

Notes. The calibrations are based on [Sanders et al. \(2025\)](#). ^(a) The metallicity range where each diagnostic can be reliably applied. ^(†) Relatively unaffected by dust reddening.

investigate the systematics associated with using different line tracers from the [Sanders et al. \(2025\)](#) calibration to infer metallicity gradients later in this Section.

We expect the contribution from the diffuse ionised gas (DIG), also known as the warm ionised medium (WIM), with $n_e \lesssim 0.1 \text{ cm}^{-3}$, $T \sim 8000$ K, in our galaxies to be minimal, although it could bias metallicity measurements in nearby disks (e.g. [Poetrodjojo et al. 2019](#); [Vale Asari et al. 2019](#); [Chevance et al. 2020](#); [Belfiore et al. 2022](#)). Our systems have, on average, $\Sigma_{\text{SFR}} \sim 10 M_{\odot} \text{ yr}^{-1} \text{ kpc}^{-2}$, about two orders of magnitude higher than in local disks where DIG dominates. As demonstrated in [Sanders et al. \(2017\)](#) and [Shapley et al. \(2019\)](#), given the observed anticorrelation between Σ_{SFR} and f_{DIG} ([Oey et al. 2007](#), and see also [Belfiore et al. 2022](#)), any DIG contribution to the spectra for our galaxies is likely to be small ($\lesssim 20\%$).

The specific line ratios used for each system in each annuli depend on the detection of the involved lines at $\text{S/N} \gtrsim 2.5$. When lines such as [O III] and H β are covered by both gratings (G235M and G395M), we select the grating that also includes the other relevant lines. For example, for R3, we use G395M for [O III] and H β for its higher S/N, if possible, but for O32, we switch to G235M to evaluate the line ratio involving [O III] and [O II], as both lines fall within this grating. This is to avoid potential differences in the absolute calibration of data from different gratings. The fluxes of the same line are consistent with each other in both gratings, but with larger uncertainty in G235M as expected.

We determine the metallicities in each radial bin using two methods. The first approach employs Bayesian inference with the emcee package ([Foreman-Mackey et al. 2013](#)) to sample the posterior probability distribution of $12 + \log(\text{O}/\text{H})$, i.e. to find the metallicity that best satisfies all calibrations at once. We name this method Method I, and provide more description in Appendix A. The inferred radial profile of these metallicities is then used to derive a gradient (denoted as ‘Method I’ in Table 3). This method is similarly applied in the spaxel-to-spaxel fitting in Sect. 5.3 to investigate azimuthal variations in metallicity.

For CRISTAL-20 and CRISTAL-22a, we utilised the metallicity maps presented in the works of [Parlanti et al. \(2025a\)](#) and [Jones et al. \(2025\)](#), respectively. In addition The metallicities were inferred from N2, R3, and O3N2 diagnostics [Parlanti et al. \(2025a\)](#), while [Jones et al. \(2025\)](#) additionally used RS32, O3S2, and O3N2, employing the calibrations from [Curti et al. \(2017\)](#) and [Curti et al. \(2020b\)](#), respectively.⁵ We share the same R3, N2, and S2, but not the RS32, O3S2, and O3N2 diagnostics.

these new observations are preferable to those relying on local analogues.

⁵ O3N2 $\equiv ([\text{O III}] \lambda 5007/\text{H}\beta)/([\text{N II}] \lambda 6583/\text{H}\alpha)$;
RS32 $\equiv ([\text{O III}] \lambda 5007/\text{H}\beta) + ([\text{S II}] \lambda \lambda 6716, 6731/\text{H}\alpha)$;
O3S2 $\equiv ([\text{O III}] \lambda 5007/\text{H}\beta)/([\text{S II}] \lambda \lambda 6716, 6731/\text{H}\alpha)$

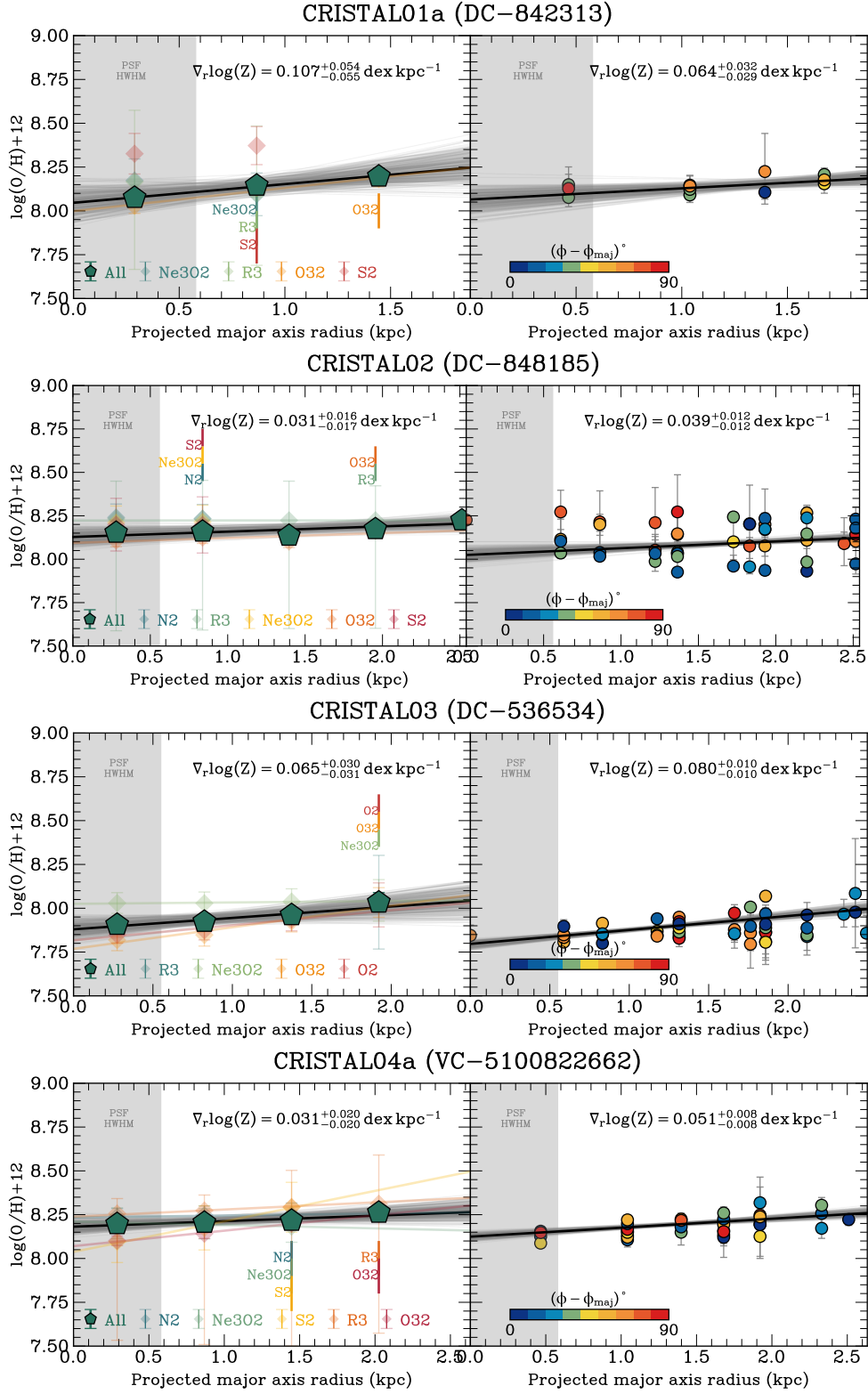


Fig. 2: Radial profiles of metallicities and their best-fit linear models (black lines). For each galaxy, the left panel shows the azimuthally-averaged profiles, where dark green pentagons with black outlines represent the metallicities derived by combining the listed line diagnostics using a Bayesian approach (Method I). The translucent grey lines are 300 random draws from the posterior distribution of the model parameters. The outermost radius at which each diagnostic is used is annotated at the corresponding location on the profile. The fainter coloured diamonds represent the metallicities obtained from individual diagnostics via Method II, while the lines in the corresponding colours show the best-fit models for each diagnostic. Similarly, the right panel shows the pixel-based metallicity profile with each data point coloured coded by its (absolute) acute azimuthal angle difference from the major axis. Line diagnostics of which only two annuli are available are shown (coloured diamonds) but not fitted.

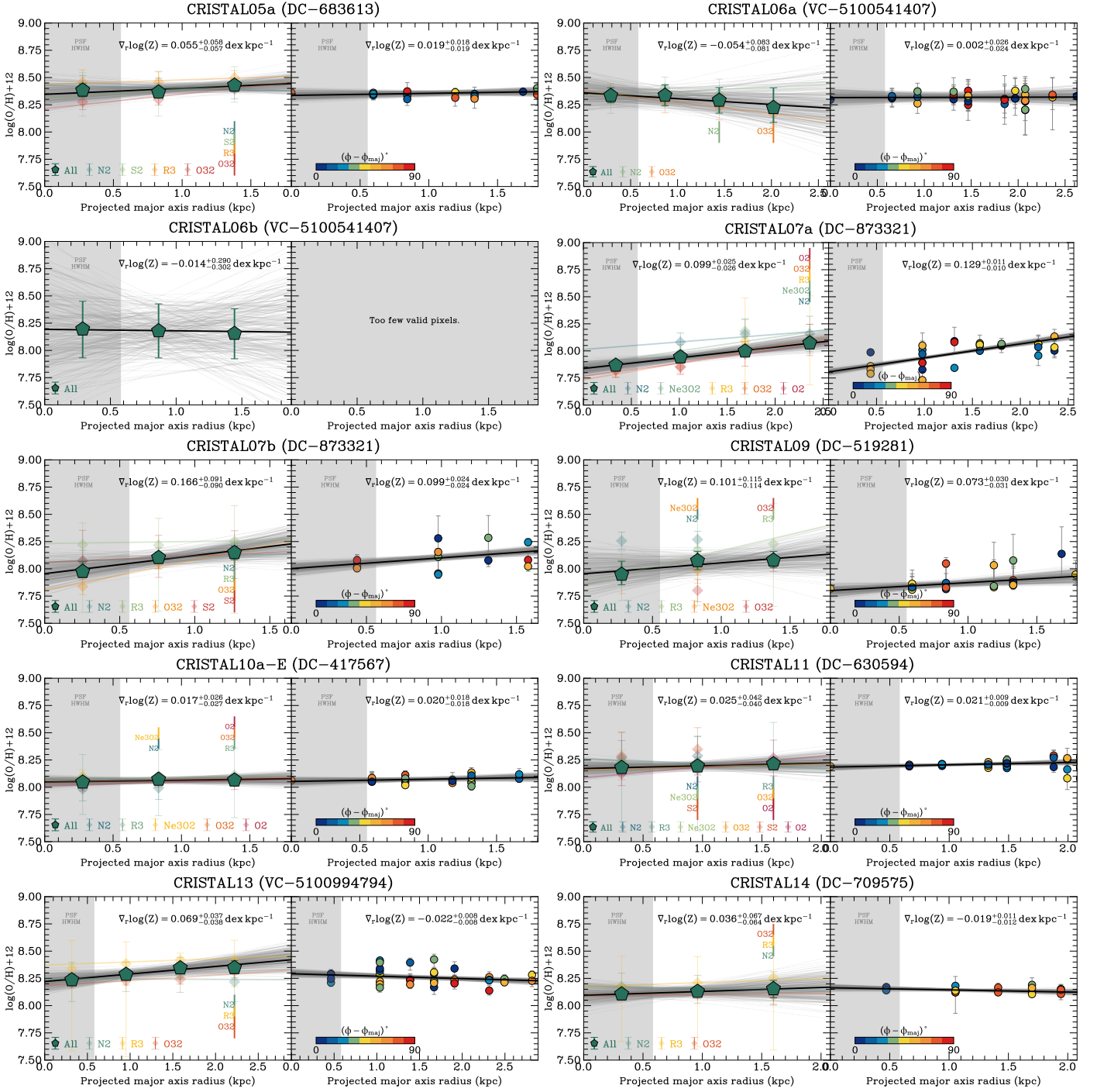


Fig. 2: (Continued.)

However, the extra indices are built from the same four bright lines, ($[O\text{III}]$, $[N\text{II}]$, $[S\text{II}]$, $H\alpha$, $H\beta$) and are therefore not independent. Within the metallicity ranges spanned by the two objects ($\log(Z) \in [8.32, 8.38]$ for CRISTAL-20 and $\log(Z) \in [8.44, 8.47]$ for CRISTAL-22a), the Curti et al. (2017, 2020b) and Sanders et al. (2025) calibrations are nearly parallel and share the same slope sign. Hence, a negative metallicity gradient would remain negative if Sanders et al. (2025) were used, and vice versa. However, the absolute metallicity values may differ by up to 0.3 dex higher (see Fig. 15 of Sanders et al. 2025).

To quantify the systematic differences between the gradients inferred from different line diagnostics, and to provide an alter-

native estimate of the uncertainties associated with the metallicity gradients, we also derive metallicities from individual line diagnostics by directly inverting the empirical calibration curves for the measured line ratios. We name this method Method II. The gradient for each diagnostic is fitted individually only when there are more than two annuli available, and the median of these gradients is reported in Table 3.

Following other $z \geq 1$ studies (e.g. Stott et al. 2014; Wuyts et al. 2016a; Carton et al. 2018), we parametrise the radial metallicity profile using a linear function,

$$\log_{10} Z(r) = \nabla_r \log_{10}(Z) \cdot r + Z_0, \quad (1)$$

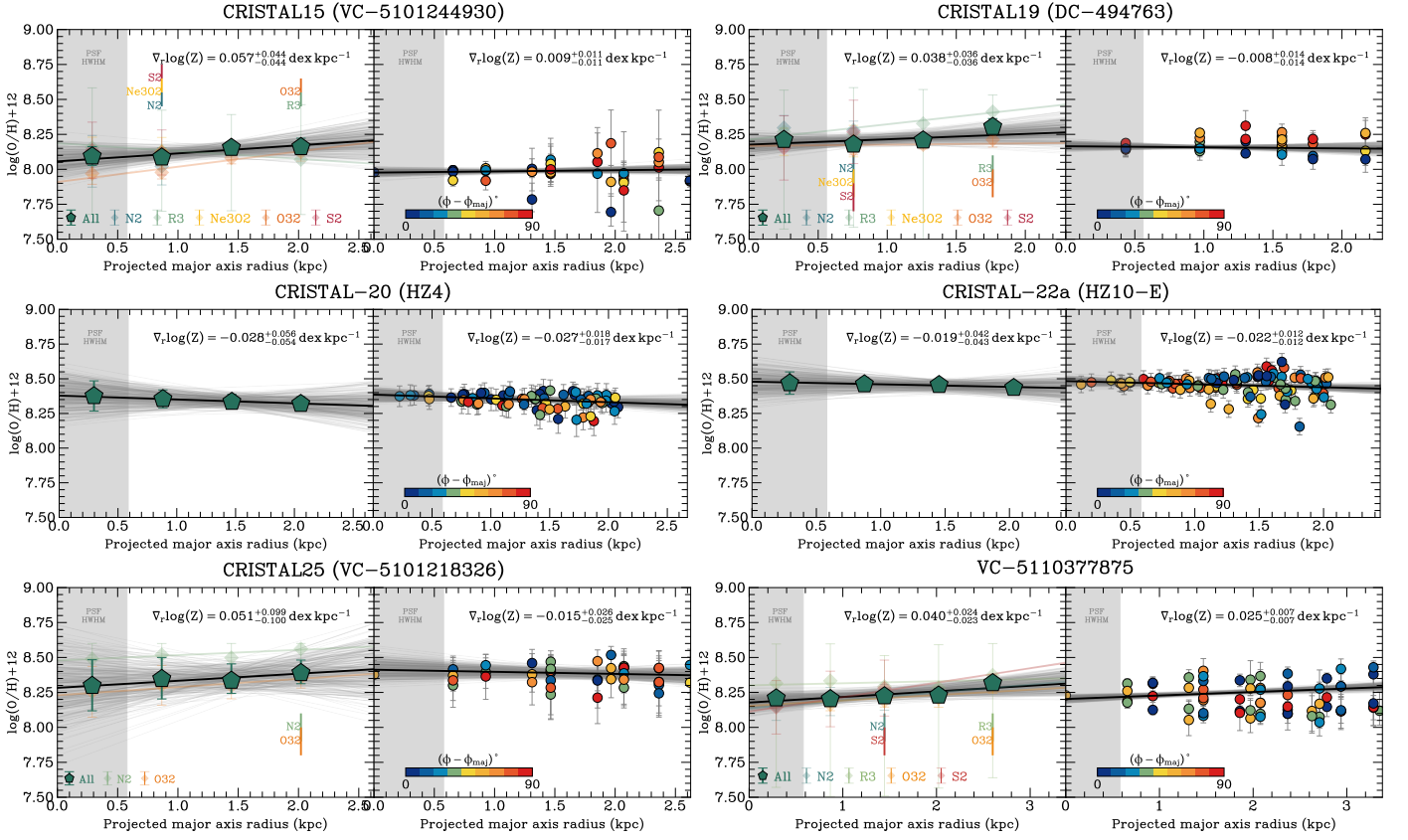


Fig. 2: (Continued.)

Table 3: Metallicity gradients inferred for the CRISTAL samples using multiple strong lines.

ID	Class. ^a	Method I ^b	Method II ^c
		(dex kpc ⁻¹)	(dex kpc ⁻¹)
01a	Non-Disk	0.107 ^{+0.054} _{-0.055}	0.107 ^{+0.028} _{-0.028}
02	Disk	0.031 ^{+0.016} _{-0.017}	0.029 ^{+0.015} _{-0.015}
03	Best Disk	0.065 ^{+0.030} _{-0.031}	0.080 ^{+0.039} _{-0.039}
04a	Non-Disk	0.031 ^{+0.020} _{-0.020}	0.041 ^{+0.058} _{-0.058}
05a	Disk	0.055 ^{+0.058} _{-0.057}	0.049 ^{+0.051} _{-0.051}
06a	Non-Disk	-0.054 ^{+0.083} _{-0.081}	-0.026 ^{+0.054} _{-0.054}
06b	Disk	-0.035 ^{+0.283} _{-0.292}	-0.004 ^{+0.032} _{-0.032}
07a	Disk	0.099 ^{+0.025} _{-0.026}	0.125 ^{+0.027} _{-0.027}
07b	Non-Disk	0.166 ^{+0.091} _{-0.090}	0.079 ^{+0.088} _{-0.088}
09	Disk	0.101 ^{+0.115} _{-0.114}	0.101 ^{+0.099} _{-0.099}
10a-E	Disk	0.017 ^{+0.026} _{-0.027}	0.020 ^{+0.018} _{-0.018}
11	Best Disk	0.025 ^{+0.042} _{-0.040}	0.025 ^{+0.046} _{-0.046}
13	Non-Disk	0.069 ^{+0.037} _{-0.038}	0.029 ^{+0.033} _{-0.033}
14	Non-Disk	0.036 ^{+0.067} _{-0.064}	0.013 ^{+0.025} _{-0.025}
15	Best Disk	0.057 ^{+0.044} _{-0.044}	0.033 ^{+0.061} _{-0.061}
19	Best Disk	0.038 ^{+0.036} _{-0.036}	0.024 ^{+0.045} _{-0.045}
20	Best Disk	-0.029 ^{+0.053} _{-0.056}	...
22a	Disk	-0.019 ^{+0.042} _{-0.042}	...
25	Non-Disk	0.051 ^{+0.099} _{-0.100}	0.044 ^{+0.029} _{-0.029}
VC-7875	Disk	0.040 ^{+0.024} _{-0.023}	0.039 ^{+0.029} _{-0.029}

Notes. ^(a) Same as Table 1 ^(b) Best-fit metallicity gradients derived from the Bayesian fitting that combines the different diagnostics listed in Table 2. ^(c) Median of the best-fit metallicity gradients derived from each individual diagnostic. The individual values of the gradients are listed in Table E.1. ^(d) Inferred from the metallicity maps in Parlanti et al. (2025a) and Jones et al. (2025).

where $\log_{10} Z = 12 + \log(O/H)$, $\nabla_r \log(Z)$ is defined as the metallicity gradient and Z_0 is the central metallicity. For both Methods, we fit the radial profiles with emcee, assuming flat priors for both $\nabla_r \log(Z)$ and Z_0 . The chains are initialised with the best-fitting solutions obtained from mpfit and then evolved with 64 walkers for 2000 steps, discarding the first 500 steps as burn-in.

The left panels of each galaxy in Fig. 2 plot the resulting best-fit metallicities profiles from Methods I and II. The values are summarised in Table 3. The typical value of measurement uncertainties is on average ~ 0.06 dex kpc⁻¹. We find that in general $\nabla_r \log(Z)$ and Z_0 obtained from Method II for individual diagnostics agree well with those from Method I, except in some cases where N2 (from Method II) prefers a flatter gradient. The gradients inferred from Method I and II, in terms of median for the latter, agree within 1σ as shown in Fig. A.2. We discuss further the difference between the two Methods in Appendix B. Henceforth, we adopt the values from Method I as our fiducial values.

The mean metallicities of our radial profiles agree within 0.3 dex with Faisst et al. (2025), which uses Sanders et al. (2024) calibrations. When comparing our metallicity gradients with those inferred by Fujimoto et al. (2025), who used the R3 and O32 diagnostics based on the same calibrations from Sanders et al. (2025), we find good agreement if we restrict our analysis to the same two diagnostics. Minor differences between our results can be attributed to the choice of apertures in multiple-component systems, e.g. CRISTAL-01a. The choices are made because of the different science goals: our study focuses on the component whose kinematics can be reliably classified and studied, whereas Fujimoto et al. (2025) emphasise the full system.

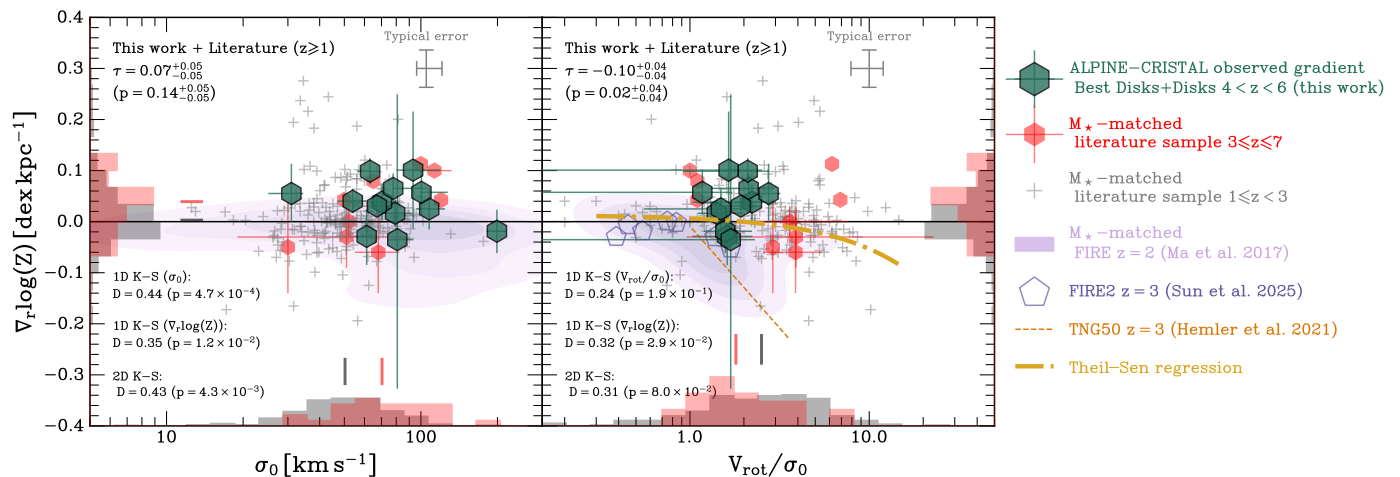


Fig. 3: Distributions of metallicity gradients, $\nabla_r \log(Z)$, as a function of the velocity dispersion, σ_0 (*left*), and the ratio of rotational velocity to velocity dispersion, V_{rot}/σ_0 (*right*), for the CRISTAL disk galaxies (green hexagons). We also show M_* -matched literature samples at $3 \leq z \leq 7$ as red hexagons, and $z < 3$ as grey crosses. The references for these literature samples are listed in Table E.4. The Kendall's τ correlation coefficients and the p -values are annotated in the top left in each panel. Histograms of the distributions of the $3 \leq z \leq 7$ and $z < 3$ samples are shown along the x - and y -axes in red and grey, respectively. The combined CRISTAL and literature sample exhibits a shallow negative correlation between $\nabla_r \log(Z)$ and V_{rot}/σ_0 , as indicated by the Kendall's τ value. The yellow dot-dashed line is the Theil–Sen median-slope regression (Sen 1968), included solely to guide the eye; it is not used in any statistical tests. In contrast, the Kendall's correlation test reveals no significant correlation with σ_0 , which could be due to the inherently shallow trend and the large scatter. However, the overall distribution of the two populations at $z < 3$ (grey histogram) and $z \geq 3$ (red histogram), a clearer distinction emerges between the $z < 3$ and $z \geq 3$ populations. Specifically, the $z \geq 3$ population tends to have higher σ_0 values and more positive metallicity gradients, whereas the $z < 3$ population has lower σ_0 values and, on average, lower metallicity gradients. This distinction is supported by the significant 2D K-S test statistics, which gives a nearly 3- σ significance level (annotated at the bottom left of each panel). The predicted trends from cosmological simulations are shown, including FIRE at $z = 2$ from Ma et al. 2017 (purple contour), FIRE2 at $z = 3$ from Sun et al. 2025 (*right*, open purple pentagons), and TNG50 at $z = 3$ from Hemler et al. 2021 (*right*, orange dashed line). While the simulations capture the slight positive and negative relationships between $\nabla_r \log(Z)$ and σ_0 and V_{rot}/σ_0 , respectively, the normalisation and steepness of these relationships differ from the observations.

Across the sample, the median $\nabla_r \log(Z) = +0.039 \pm 0.010 \text{ dex kpc}^{-1}$ (standard deviation = 0.053). All galaxies except CRISTAL-06a, 06b, 20 and 22a have positive metallicity gradients. However, there are no galaxies with $\nabla_r \log(Z) > +0.05 \text{ dex kpc}^{-1}$ at 3σ level, and only three galaxies at 1σ . If we consider strictly flat metallicity gradient, i.e. $\nabla_r \log(Z) = 0 \text{ dex kpc}^{-1}$, there are 11 galaxies with $\nabla_r \log(Z) > 0 \text{ dex kpc}^{-1}$, but only at 1σ level. For CRISTAL-06a, 06b, 20 and 22a, none of them have gradients significantly steeper than $-0.05 \text{ dex kpc}^{-1}$ (typical values of the Milky Way and local spirals) and they are consistent with 0 dex kpc^{-1} at 1σ level. For CRISTAL-20 and -22a, we have verified the sign of the gradients would not reverse if Sanders et al. (2025) calibration is used.

For the galaxies that exhibit mild positive gradients, the gradients could be produced by (at least) two non-exclusive mechanisms: (1) the accretion of metal-poor filaments that stream gas penetrating the galaxy halo and deliver pristine gas directly to the inner kiloparsec (Dekel et al. 2009; Ceverino et al. 2016), (2) galactic outflows with high mass loading factors could preferentially remove metals from the central regions, and a fraction of this enriched gas could cool and be re-accreted at the outer regions of the galaxy, the so-called galactic fountain (Gibson et al. 2013; Ma et al. 2017), although direct evidence for metal-rich fountains at $z > 4$ is still lacking. These processes could lead to an increase in the outer metallicity, resulting in positive metallicity gradients.

The flatness of our observed metallicity gradients could be potentially an observational effect of angular resolution (Yuan et al. 2011; Wuyts et al. 2016b). We will explore whether beam smearing could contribute to the shallow gradients observed in most of our sample in Sect. 6.

Notably, the three galaxies with the steepest gradients are CRISTAL-01a, 07a and 07b, which are known to have an immediate neighbour within $\sim 10 \text{ kpc}$. CRISTAL-01a resides in a dense region with multiple companions and a massive neighbour, SMG J1000+0234 (Jiménez-Andrade et al. 2023; Solimano et al. 2024, 2025; Rubet et al. 2025). The observed kinematic features suggest that this system may be in the later stages of a merger, and the misaligned velocity gradient hints at gas inflow triggered by the merger (Lee et al. 2025a). CRISTAL-07a and 07b is an interacting pair, with CRISTAL-07a retaining a lot of its disk rotation signatures.

The interacting nature of CRISTAL-01a, 07a, and 07b may contribute to their observed positive metallicity gradients as found at lower redshifts (e.g. Kewley et al. 2010; Rupke et al. 2010b; Queyrel et al. 2012; Carton et al. 2018; Wang et al. 2022), and also reported in one case at $z \sim 8$ by Venturi et al. (2024). However, not all interacting pair systems in our sample exhibit positive gradients; for example, CRISTAL-06a and 06b have slight negative gradients instead. The uncertain stage of merger for these systems complicates a direct association between interaction and metallicity gradients.

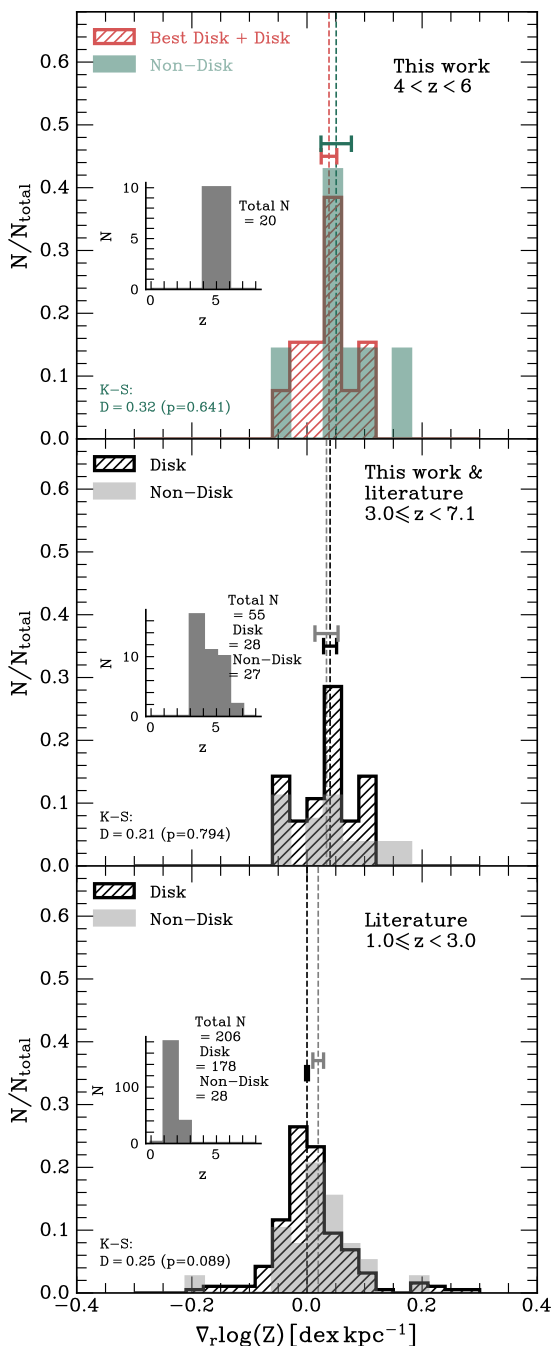


Fig. 4: Metallicity gradients in disk and non-disk subsets of our sample (*top*) and compiled stellar mass-matched sample from literature at $3 < z \lesssim 8$ (*middle*) and $1 < z < 3$ (*bottom*). The median values of the distributions are indicated by the vertical dashed line of the corresponding colours, and similarly for the errors of the median (obtained by bootstrapping) which are represented by the horizontal error bars of the same colour. The literature references are listed in Table E.4.

5. Gas-phase abundance gradients and their potential drivers

In this section, we will discuss the values of $\nabla_r \log(Z)$ for different sub-populations in our sample.

5.1. Metallicity gradients in disks

Studies of star-forming disks at cosmic noon have found that galaxies with higher gas velocity dispersions σ_0 tend to have flatter and in some cases even positive radial metallicity gradients (Queyrel et al. 2012; Jones et al. 2013; Gillman et al. 2021; Leethochawalit et al. 2016; Wang et al. 2022). Consistent with this trend, the metallicity gradients exhibit a mild anti-correlation with the ratio V_{rot}/σ_0 , where V_{rot} is the rotation velocity.⁶ Both trends between metallicity gradients and σ_0 and V_{rot}/σ_0 observed in the literature are illustrated in Fig. 3.

We investigate the relationships between metallicity gradients, $\nabla_r \log(Z)$, and the gas-phase velocity dispersion, σ_0 , as well as V_{rot}/σ_0 , from [C II] for the 13 disk galaxies (Fujimoto et al. 2020; Lee et al. 2025a) and samples compiled from the literature at $z \gtrsim 1$ in Fig. 3. The literature samples included are listed in Table E.4 (those with kinematics references, and see discussion in Appendix C). We select galaxies that fall within the mass range of our sample. The resulting distribution of stellar masses is shown in Fig. E.1. The stellar mass values are taken from the literature, which we discuss in detail in Sect. 5.4.

The literature data were obtained using a variety of instruments, ranging from ground-based to space-based, and from grism to IFU spectrographs, with widely varying spatial and spectral resolutions. Furthermore, the metallicities were inferred using different strong-line diagnostics and calibrations. However, as discussed in Appendix C, the current sample size does not allow a more unified sample selection, so we chose to retain the literature sample as is, with only the stellar mass selection. To maximise statistical coverage in our kinematics measurement, we do not unify the gas phase from which the measurement is taken. In addition, the different beam-smearing correction method and modelling methodologies (Übler et al. 2019; Lee et al. 2025b; Wisnioski et al. 2025) could introduce systematic scatter in the kinematics data, which we could not correct here. Nevertheless, since the kinematic data are predominantly derived from IFU observations, the known bias in using long-slit or grism data (Übler et al. 2019) is mostly mitigated.

We find a shallow yet statistically significant ($p < 0.05$) negative correlation between $\nabla_r \log(Z)$ and V_{rot}/σ_0 among the CRISTAL disks and literature values, with a Kendall's τ correlation coefficient of $-0.10^{+0.04}_{-0.04}$. The quoted uncertainties are obtained from the empirical distributions of Monte-Carlo bootstrapping for 1000 resamples. To further verify the trend is not driven by one object, we applied jack-knife resampling that gives a distribution of $\hat{\tau}$ values whose [5, 95]th-percentile fall within $[-0.13, -0.07]$. These intervals lie well within the confidence intervals estimated from bootstrapping.

Observations of MS SFGs from $z \lesssim 8$ to $z = 1$ suggest that V_{rot}/σ_0 increases with cosmic time (Fig. 9 in Lee et al. 2025a), a trend that is also seen in simulations (e.g. Pillepich et al. 2019; Sun et al. 2025). Therefore, the correlation between $\nabla_r \log(Z)$ and V_{rot}/σ_0 likely reflects the cosmic evolution of $\nabla_r \log(Z)$ with redshift, where $\nabla_r \log(Z)$ becomes more negative towards lower redshift, as discussed in Fujimoto et al. (2025) in the context of our sample and Curti et al. (2020a); Venturi et al. (2024) for a general discussion.

Since V_{rot}/σ_0 is an indicator of disk maturity in terms of rotational support, the coherent picture of metallicity gradients decreasing with both V_{rot}/σ_0 and cosmic time implies that disk maturity plays a dominant role in driving the negative metallicity gradient, among also other evolving variables with red-

⁶ As discussed in Sect. 6.1 in Lee et al. (2025a), the definition and methodology used to derive V_{rot} and σ_0 varies across literature.

shift. This is consistent with simulations, such as those presented in Ma et al. (2017); Bellardini et al. (2021); Sun et al. (2025), which show that disks become increasingly rotationally supported over time and consequently, suppress radial mixing of metals, leading to a gradual steepening of the radial metallicity gradients over time.

In contrast, no discernible correlation is observed between $\nabla_r \log(Z)$ and σ_0 , as indicated by a Kendall's τ of 0.06 and a p -value = 0.18, which rules out any strong trends. The lack of trend between $\nabla_r \log(Z)$ and σ_0 could be attributed to the inherently shallow trend as predicted by FIRE simulation (for $z = 2$, Ma et al. 2017), and the large scatter preclude any trends. Nevertheless, the overall distribution of the two populations at $z < 3$ and $z \geq 3$, a clearer distinction emerges between the $z < 3$ and $z \geq 3$ populations. Observationally, σ_0 exhibits a decreasing trend with decreasing redshift (Fig. 9 in Lee et al. 2025a). Consequently, the distinction between the $z < 3$ and $z \geq 3$ populations could be, in part, reflecting the trend between σ_0 and the metallicity gradient. This distinction is supported by the two-dimensional Kolmogorov-Smirnov (K-S) D-statistics (Peacock 1983; Fasano & Franceschini 1987; Press et al. 2007) test statistics, which gives a nearly $3\text{-}\sigma$ significance level. For reference, the D-statistics from the 1D K-S test of the galaxies in our sample for each variable are also provided in Fig. 3.

The σ_0 and V_{rot}/σ_0 values could be used to gauge the local stability of a gaseous disk through the Toomre Q parameter, in which $Q \propto (\sigma_0/V_{\text{rot}})f_{\text{gas}}^{-1}$ (e.g. Genzel et al. 2011).⁷ The lower the Q , the more unstable the disk against local collapse. CRISTAL galaxies have high gas fractions, $f_{\text{gas}} \approx 0.5$ on average, and a median $Q \sim 0.6$ (Lee et al. 2025a), close to the critical value for a marginally stable thick disk (e.g. Behrendt et al. 2015). In such low- Q conditions, the disk is expected to fragment into giant, star-forming clumps that could contain $\sim 7\%$ of the total stellar mass (Förster Schreiber & Wuyts 2020, and references therein). The gravitational torques exerted by these clumps, together with global non-axisymmetric modes, drive radial gas inflow that can efficiently flatten the metallicity gradient (e.g. Bournaud et al. 2007, 2011; Goldbaum et al. 2016). Simulations suggest, however, that only the most massive and densest long-lived clumps are likely to survive the inward migration across the disk (Dekel et al. 2022; Ceverino et al. 2023). Observations have yet to provide clear evidence for such clump migration (Claeyssens et al. 2025; Kalita et al. 2025).

Morphologically, many CRISTAL galaxies exhibit pronounced clumpy structure in rest-frame optical JWST/NIRCam images (Lee et al. 2025a, see also R. Herrera-Camus et al., in prep.), whereas their stellar-mass distributions, inferred from resolved SED (spectral energy distribution) modelling (Li et al. 2024; Lines et al. 2025) and ALMA [C II] data (Ikeda et al. 2025; Lee et al. 2025a), appear relatively smooth.

Most of the disks in our sample lack a massive bulge, as inferred from kinematic analysis (Lee et al. 2025a). The flat metallicity gradients observed in these disks lend additional support for the absence of a strong and mature bulge component at $4 < z < 6$.

The empirical trends between metallicity gradients and σ_0 and V_{rot}/σ are broadly reproduced by cosmological simulations from FIRE and TNG50 (Ma et al. 2017; Hemler et al. 2021) for $z \geq 2$ (see also the analytical model by Sharda et al.

2021b). They suggest that a galaxy requires a highly rotation-dominated cold disk to develop a steep negative metallicity gradient, whereas galaxies lacking ordered rotation tend to exhibit flat gradients. More recently in Sun et al. (2025), they also found galaxies with weak rotational support ($V_{\text{rot}}/\sigma_0 \lesssim 1$) are more likely to develop positive metallicity gradients. In these simulations, the observed correlation with V_{rot}/σ_0 is driven by the effective redistribution of metal-rich gas in dispersion-dominated galaxies through processes such as rapid gas infall, which flattens the metallicity gradients.

5.2. Metallicity gradients in disks versus non-disks

Figure 4 shows the distribution of $\nabla_r \log(Z)$ of disks and non-disks of our sample. We find no significant distinction between disks and non-disks as classified in Lee et al. (2025a), with median $\nabla_r \log(Z) = +0.038 \pm 0.013 \text{ dex kpc}^{-1}$ and $+0.051 \pm 0.026 \text{ dex kpc}^{-1}$, respectively, with a negligible difference of $< 1\sigma$ level, and a K-S test does not indicate the two populations are distinct with score of 0.32 ($p = 0.64$).

We also compare with the disks and non-disks in the literature listed in Table E.4. Galaxies are classified as disks or non-disks following the criteria adopted in the original studies, using either (i) their kinematic designations ('rotating' versus 'non-rotating') or (ii) their morphological classifications from imaging data, including *Hubble* Space Telescope (HST) observations.

For the literature sample at $3 \leq z \leq 7$, we find no significant distinction between the disk and non-disk populations, with an insignificant difference in their median values (disk: $+0.040 \pm 0.011 \text{ dex kpc}^{-1}$, non-disk: $+0.034 \pm 0.020 \text{ dex kpc}^{-1}$). When combining our sample with the existing literature at $3 \leq z \leq 7$ (Fig. 4), increasing the number of objects from 35 to 55, the difference between the disk and non-disk populations remains negligible in terms of median difference, with high p -value = 0.80 from K-S test.

On the other hand, a more noticeable difference in metallicity gradients between disks and non-disks is observed at $1 \leq z < 3$ in our compiled sample of 206 galaxies shown in Fig. 4, with median values of $0.000 \pm 0.003 \text{ dex kpc}^{-1}$ and $0.0195 \pm 0.009 \text{ dex kpc}^{-1}$, respectively, although this difference in median values is only significant at 2σ level. This significance is comparable to that reported in the 21 disk and non-disk samples in SINS/zC-SINF at $z \sim 2$ by Förster Schreiber et al. (2018). Similarly, Gillman et al. (2021) found no difference in the metallicity gradients between morphologically irregular and disk galaxies in a sample of ≈ 650 SFGs at $z \sim 1$, albeit based on HST data available at the time.

The lack of a strong distinction between disks and non-disks in our sample may be attributed to the ambiguous nature of non-disks, as discussed in Lee et al. (2025a). Non-disks could be potential mergers or disks with strong non-circular motions that are not resolved with the current data quality. The merger stage for the former scenario is largely unknown, while the latter scenario would make non-disks less distinct from disks.

Furthermore, the overall high molecular gas fraction ($f_{\text{gas}} = M_{\text{gas}}/(M_{\text{gas}} + M_{\star}) \gtrsim 50\%$) of the sample with little systematic difference between disks and non-disks (Lee et al. 2025a) imply rapid and efficient inward gas streaming from the pristine circum-galactic medium (CGM) and inter-galactic medium (IGM), as well as minor mergers, which feed the galaxy to maintain a large gas fraction (e.g. Tacconi et al. 2020). As discussed in Sect. 5.1, the gas-rich nature of these systems could induce efficient formation of clumps, and their migration and further gas inflow driven by tidal torques exerted on the gas could flat-

⁷ An approximation neglecting the contribution from the stellar and other gaseous components, a multi-component or effective Q would give a slightly different numerical value but the same qualitative behaviour (Wang & Silk 1994; Romeo & Falstad 2013).

ten metallicity gradients. Nevertheless, observational evidence remains unclear on whether the clumps can actually survive this migration (Claeysens et al. 2025; Kalita et al. 2025).

Further supporting the above picture is the growing evidence for rapid radial gas inflow ($v_{\text{inflow}} \approx 50 \text{ km s}^{-1}$) in star-forming disks at $z \sim 2$ (Genzel et al. 2023; Huang et al. 2025; Pastras et al. 2025, C. Pulsoni et al., in prep.). This would imply material migrates over a flow (dynamical) time of $< 100 \text{ Myr}$, much shorter than that of local disks. Because this inflow timescale is shorter than, or at best comparable to, the gas-consumption (star-formation) timescale ($\lesssim \text{Gyr}$, Tacconi et al. 2020), relatively small in-situ metal enrichment can occur during a single episode of inward transport. Consequently, these galaxies are expected to develop relatively flat metallicity gradients, and with little azimuthal variations (Petit et al. 2015), which we will investigate further in Sect. 5.3.

Comparable gradient flattening could also take place in interacting and merging systems at all epochs, where tidal torques likewise drive efficient radial gas mixing (e.g. Rupke et al. 2010b; Croxall et al. 2015; Wang et al. 2019; Venturi et al. 2024). Hence, both high-redshift gas-rich disks and mergers may share a common, rapid, large-scale gas redistribution that suppresses steep abundance gradients.

The high gas fraction at $z \sim 5$ also sustain elevated star-formation rates compared to the local Universe. The ensuing strong stellar feedback launches outflows that could redistribute metals into the outer disk (Gibson et al. 2013; Übler et al. 2014; Tissera et al. 2022). Subsequent re-accretion of this material, together with turbulent mixing, is expected to further moderate radial variations in chemical composition, which could ultimately diminish the difference between disk and non-disk galaxies at $4 < z < 6$.

5.3. Azimuthal variations

As found in many $z \sim 1-3$ galaxies, metallicity distribution is often very irregular, with considerable local variations even on kpc scales (e.g. Förster Schreiber et al. 2006, 2018; Gillman et al. 2022), as well as in simulations (Bellardini et al. 2021). These irregularities may reflect the non-symmetric processes such as chaotic accretion, feedback, gravitational instabilities and transport processes during these early galaxy evolution phases. The presence of more metal-poor clumps or unresolved small companions will also introduce local variations in metallicities. Hence, averaging large azimuthal variations into the same radial bins could wash out such features and result in an apparently flat radial gradient.

To quantify the azimuthal variations in our sample, we apply the same procedure used for the annular-binned profile in Sect. 4, but on a spaxel-to-spaxel basis. We select only those pixels where the line ratios exceed the 2.5σ limit (see Sect. 8.3 of Förster Schreiber et al. 2018), which implies the line flux of the fainter line (e.g. H β in R3) must also exceed 2.5σ . Note that the 2.5σ threshold is applied on the line ratio, which is a more stringent requirement than the same threshold on the individual line fluxes; the former is effectively equivalent to raising the per-line S/N threshold much above 2.5σ .

Here we focus on oxygen-based diagnostics (e.g. O32) if available, which typically have higher S/N and larger radial coverage. For CRISTAL-06a and 06b, only N2 is available. The Fig. 2 shows the per-pixel metallicities profile for our sample, the data points are colour-coded by their acute azimuthal angle difference relative to the position angle of the morphological major axis ($\Delta\phi = |\phi - \phi_{\text{maj}}|$).

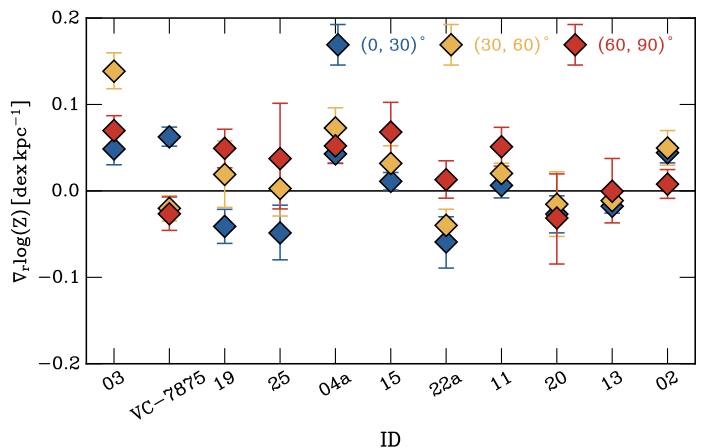


Fig. 5: Metallicity gradients inferred in three azimuthal bins: $[0^\circ, 30^\circ)$ (blue), $[30^\circ, 60^\circ)$ (yellow), and $[60^\circ, 90^\circ)$ (red). The galaxy IDs are sorted from left to right by their azimuthal variations in terms of standard deviation.

We then fit the metallicity gradients for pixels within an azimuthal bin of $\Delta\phi = 30^\circ$, dividing the galaxies into three bins spanning $[0, 90]^\circ$. Out of the 20 galaxies in our sample, 11 have sufficient pixels within an azimuthal bin for this measurement. There are typically 17 spaxels fall within each azimuthal bin. Fig. 5 presents the distribution of metallicity gradients for the 11 galaxies in each bin, and Table E.2 summarises the values. The scatter among the azimuthal-binned values around their mean values is relatively low, averaging $0.02 \text{ dex kpc}^{-1}$, with a maximum scatter of $0.04 \text{ dex kpc}^{-1}$ observed for CRISTAL-03, 19, 25 and VC-7875, which is still smaller than the typical measurement uncertainties of the annular-binned gradients of $\sim 0.06 \text{ dex kpc}^{-1}$ from Method I in Sect. 4.

Comparing the mean difference between the azimuthally-binned above and annular-binned metallicity gradients inferred from Method I, we find that none of the galaxies show a significant deviation from the annular-binned metallicity gradient, with no galaxies showing a mean difference exceeding 3σ . Only four galaxies (CRISTAL-03, 04a, 13, and VC-7875) show a difference at 1σ level, indicating there could be mild azimuthal variations these cases, given the uncertainties of this pixel-based method.

To assess the azimuthal variation in the whole sample, especially in cases where the azimuthal binning method above could not be applied, we fit the radial profile of these per-pixel metallicities in the full azimuthal range, following e.g. Förster Schreiber et al. (2018), using the same procedure as Method I in Sect. 4. The derived gradients are presented in Fig. 2 on the right of each panel. Fig. 6 compares the gradients from Method I and the pixel-based metallicity profiles derived here.

In all cases, the two profiles agree within 1σ , indicating that there are generally no strong azimuthal variations in the radial profiles. The pixel-based metallicity gradients are only slightly flatter than those derived from azimuthal averaging, with a mean $\nabla_r \log(Z)$ of $+0.027 \pm 0.007 \text{ dex kpc}^{-1}$, compared to $+0.043 \pm 0.019 \text{ dex kpc}^{-1}$, with a marginal difference of $\approx 1\sigma$. Such small discrepancy could be attributed to several factors, including the different radial coverage of the azimuthally-averaged and pixel-based metallicity gradients, and the inherently light-weighted nature of the azimuthally-averaged method.

Overall, we do not find strong azimuthal variations that are statistically significant above the measurement uncertain-

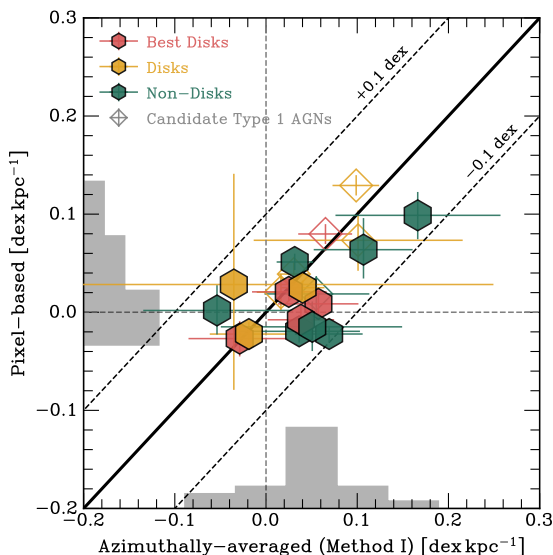


Fig. 6: Comparison between the azimuthally-averaged (from Method I) and pixel-based metallicity gradients. The disks and non-disks classified in Lee et al. (2025a) are shown in pink/yellow and green, respectively. The candidate Type-1 AGNs identified in Ren et al. (2025) are marked with the diamond symbol.

ties. However, four galaxies, namely CRISTAL-03, 19, 25, and VC-7875, exhibit slightly stronger azimuthal variations compared to the rest of the sample. CRISTAL-03 was identified by Ren et al. (2025) as candidate Type-1 AGN because their spectra exhibit broad Balmer components. However, in their BPT diagrams, as well as in diagnostics based on $\text{He II } \lambda 4686$ (Shirazi & Brinchmann 2012) and the $[\text{O III}] \lambda 4363/\text{H}\gamma$ ratio — the latter being more suitable at high- z (Mazzolari et al. 2024), CRISTAL-03 consistently lies around the star-forming/composite locus, showing no significant excess of hard ionising photons. VC-7875 is a disturbed disk galaxy, as identified by Fujimoto et al. (2020), and further supported by JWST NIRCcam imaging data that it is part of an interacting system. For CRISTAL-25, Li et al. (2024) suggested the potential presence of a Type 1 AGN based on NIRCcam broadband photometry, which hinted at an excess of flux from the broad component of $[\text{Mg II}] \lambda 2798$ and $\text{H}\beta + [\text{O III}] \lambda 5007$. However, our G235M data are unable to confirm this due to the low S/N of $\text{H}\beta + [\text{O III}]$ (even $[\text{O III}] \lambda 4959$ is barely detected), and $[\text{Mg II}]$ being shifted out of the spectral coverage. For CRISTAL-19, a disk system, the origin of the mild azimuthal variation is unclear.

The overall lack of strong azimuthal variations is also found in some studies in the local Universe (Kreckel et al. 2020), which, despite having much better statistics based on over hundreds of H II regions, report RMS scatter of $\lesssim 0.05$ dex after removing the large-scale gradient, suggesting a high level of chemical homogeneity over large spatial scales. Williams et al. (2022) also finds no clear systematic enrichment in the spiral arms, which is somewhat unexpected, given that the primary source of oxygen is Type II supernovae, which are typically more densely populated along the spiral arms.

The lack of azimuthal variations in disks could be explained if the turbulent mixing timescale is much shorter than the orbital time required for differential rotation to wind non-axisymmetric abundance patterns into tight spirals. The resulting shear-mixing could therefore erase most of the contrast, resulting in the

weak azimuthal scatter observed at fixed galacto-centric radius (Yang & Krumholz 2012). Given that the disk galaxies in our sample have higher velocity dispersions, averaging $\sim 70 \text{ km s}^{-1}$, than local disks, the turbulence-driven mixing is likely even more efficient, which could explain the absence of strong azimuthal variations.

Nevertheless, we are cautious that observational limitations may also explain why the majority of the galaxies do not exhibit a large azimuthal variation in metallicities. A single pixel in the NIRSpc IFU of size $0''.1$ corresponds to a physical scale of $0.5\text{--}0.7 \text{ kpc}$ at redshifts $z = 4$ to 6. Because our observations employ only the standard 2-point dither pattern (with the exception of CRISTAL-01, 20 and 22a see Fujimoto et al. 2025; Jones et al. 2025; Parlanti et al. 2025a), the data provide only modest sub-pixel sampling. It is further exacerbated by the limited angular resolution of a similar order, which altogether limits our view to the non-axisymmetric features that may bring about local metallicity variations, such as clumps (e.g. Wang et al. 2017; Estrada-Carpenter et al. 2025; Sok et al. 2025; Parlanti et al. 2025b) and spiral arms, which have been observed in some other local studies (Vogt et al. 2017; Bresolin et al. 2025) and simulations (Spitoni et al. 2019; Orr et al. 2023). Hence, it is difficult to confirm or rule out the presence of these features as drivers of metallicity variations (Genzel et al. 2011; Newman et al. 2012; Khoperskov et al. 2023) within the physical scales probed by our current data.

5.4. Mass and sSFR

A positive correlation between sSFR and radial metallicity gradients was identified by studies of SFGs at cosmic noon (e.g. Stott et al. 2014; Wuyts et al. 2016a; Curti et al. 2020b). A negative correlation with M_* (e.g. Wuyts et al. 2016a; Wang et al. 2020; Cheng et al. 2024, but see also Li et al. 2025a for $M_* \lesssim 10^9 M_\odot$ at $z > 6$) has also been found. In general, these studies found that low-mass and high-sSFR galaxies tend to have flatter to even positive gradients, as shown in Fig. 7. This may be due to the higher mass loading of starburst-driven galactic winds at early times in those low-mass systems, which eject metal-enriched gas from galaxy centres and may deposit it at larger radii. In simulations, this is attributed to efficient feedback in such systems, which keeps them in the ‘bursty’ star formation mode (Ma et al. 2017).

The stellar masses and SFRs were derived from SED fitting using various tools in the literature. For the single literature source that adopted the Salpeter IMF, we scale its stellar mass and SFR down by a factor of 1.7 to place them on the Chabrier IMF (Speagle et al. 2014). For the 17 galaxies already adopting a Kroupa IMF, no adjustment is applied since the Kroupa-Chabrier offset is negligible relative to our error budget.

We cannot confirm any significant trends between metallicity gradients and M_* or sSFR in our sample, with low Kendall’s τ correlation coefficients ($\tau \lesssim 0.15$, $p \gg 0.05$). We do not observe any significant correlation with the surface density of star formation, Σ_{SFR} either. Even when combining our sample with literature samples compiled at $z > 3.0$ (Table E.4), which extend to lower stellar masses ($\log(M_*/M_\odot) < 9.0$) and higher sSFR values ($\log(\text{sSFR}/\text{yr}^{-1}) \gtrsim -8$), the negative and positive trends with M_* and sSFR, respectively, are only marginally stronger. However, the statistical significance of these trends remains weak, as indicated by the low Kendall’s τ values and high p -values annotated in Fig. 7.

Comparing our results with cosmological simulations, the lack of a trend between $\log(M_*)$ and metallicity gradient is not

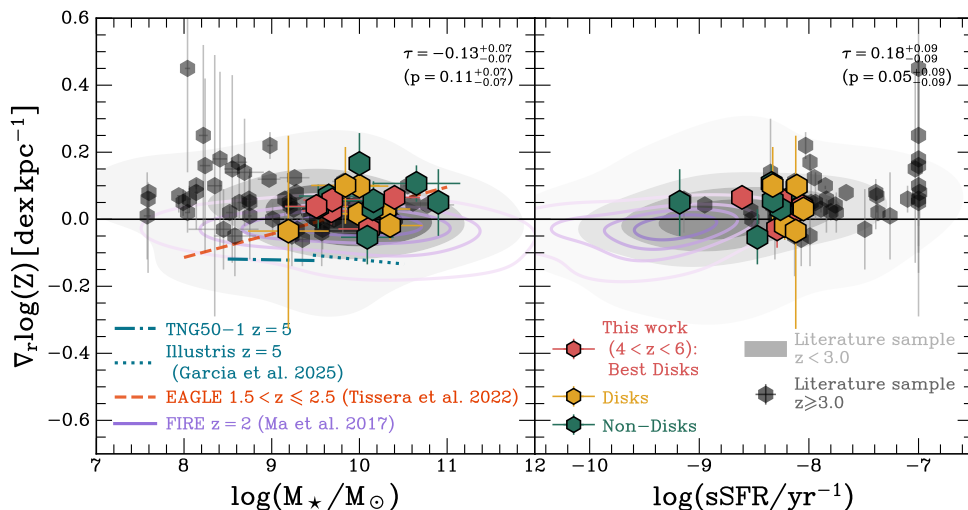


Fig. 7: Observed metallicity gradients as a function of M_* (left) and specific star formation rate (sSFR, right). The literature samples at $z < 3.5$ and $z \geq 3.5$ are represented by black contours and black hexagons, respectively. The references for the literature sample are listed in Table E.4. Predictions from the cosmological simulations TNG50-1 and Illustris (Garcia et al. 2025) are plotted as dot-dashed and dotted blue lines, respectively. Additionally, we show the trends from other simulations at $z \approx 2$, including EAGLE (Tissera et al. 2022) as an orange dashed line (left only) and FIRE (Ma et al. 2017) as purple contours. The values from FIRE2 (Sun et al. 2025) are within the FIRE contours, therefore not plotted. The Kendall’s τ correlation coefficient and the p -value for the combined distribution of our sample and the literature sample are annotated in the top right corner of each panel.

entirely unexpected. At $z \leq 2.5$, both the FIRE (Ma et al. 2017) and FIRE2 (Sun et al. 2025) simulations found very shallow to no correlation with $\log(M_*)$. Given the uncertainties present in our data and the literature, constraining a weak trend like this remains challenging. Although our results show a better match with the EAGLE simulation within the mass range of our sample, the relationship with M_* is not well reproduced for the literature-compiled sample at $z \geq 3$ across a broader mass range, particularly at the low-mass end. However, studies by Tissera et al. (2022) (EAGLE) and Hemler et al. (2021) (TNG) do suggest that lower-mass galaxies exhibit greater fluctuations, and our current limited sample may be too small to capture the full scatter. A more recent study by Garcia et al. (2025) found that the TNG50-1 and Illustris simulations at $z = 5$ capture the flat dependence on M_* , but predict an overall more negative gradients than our observed results for our mass range.

Since the M_* and sSFR we are comparing here are primarily SED-based quantities, and could give rise to systematic scatter due to different assumptions for example on the star-formation history, and SED-modelling tools (Pacifci et al. 2023), we also compare with SED-independent quantities such as dynamical mass (M_{dyn}) and gas mass (M_{gas}). Within our sample, we do not find strong correlations between the metallicity gradients and the dynamical mass and the gas mass or fraction (either $M_{\text{gas}}/M_{\text{baryon}}$ or M_{gas}/M_*) measured in Lee et al. 2025a), with Kendall’s $\tau \lesssim 0.3$ and a large p -value. Note that we only have dynamical mass for disks. In mergers, the M_{dyn} inferred from the integrated line width lacks physical meaning. We could not expand the M_{gas} comparison much beyond our own sample because most galaxies lack direct M_{gas} measurements, nor did we. If we use V_{rot} as a proxy for the M_{dyn} of literature disks, we find Kendall’s $\tau = -0.09^{+0.05}_{-0.04}$ and p -value of $0.05^{+0.05}_{-0.04}$, no compelling trend.

6. Effects of beam smearing

The observed shallow gradients in our sample could be partly caused by observational effects (Yuan et al. 2011; Wuyts et al. 2016b; Carton et al. 2018; Acharyya et al. 2020). Convolution of the intrinsic line flux distribution with the PSF acts as a spatial blurring kernel that reduces local contrast and any kind of gradients would be suppressed and appear shallower, an effect known as beam smearing. Intuitively, the steeper the intrinsic gradient and the broader the PSF relative to the size of the galaxy, the stronger the flattening. To the extreme, for a flat gradient, beam smearing has no effect.

To quantify the beam-smearing effect and understand the impact on our measurements, we generate 1500 mock galaxies with a given intrinsic metallicity gradient ranging between $\nabla_r \log(Z) \in [-0.2, +0.2]$ dex kpc $^{-1}$. The mock data cubes are built out of exponential disk models using `DysmalPy`⁸ (Davies et al. 2004b,a; Cresci et al. 2009; Davies et al. 2011; Wuyts et al. 2016b; Lang et al. 2017; Price et al. 2021; Lee et al. 2025b) with parameters listed in Table 4. Since the purpose here is to test the effect of beam-smearing on metallicity gradient, we set the mass model to $\log(M_{\text{bary}}/M_{\odot}) = 10.5$, where M_{bary} is the total baryonic mass, and $R_{\text{e,disk}} = 2$ kpc which are representative of the galaxies in our sample (Herrera-Camus et al. 2025). We do not vary these physical properties for the mock models, but vary only the ratio of the effective radius to that of the beam size, as well as the S/N ratio. The inclination is fixed at 20° because, as demonstrated by Wuyts et al. (2016b), in practice, the ellipticity of the apertures is typically tailored to match the observed isophotes, and hence variations with respect to inclination is less relevant.

We add [O II], [Ne III], H β and [O III] line emissions assuming a linear radial gradient (Eq. 1), such that the line intensity of H β , [O II] and [Ne III] relative to [O III] are controlled via the R3, O32 and Ne3O2 relations listed in Table 2, assuming the spectra have

⁸ <https://www.mpe.mpg.de/resources/IR/DYSMALPY>

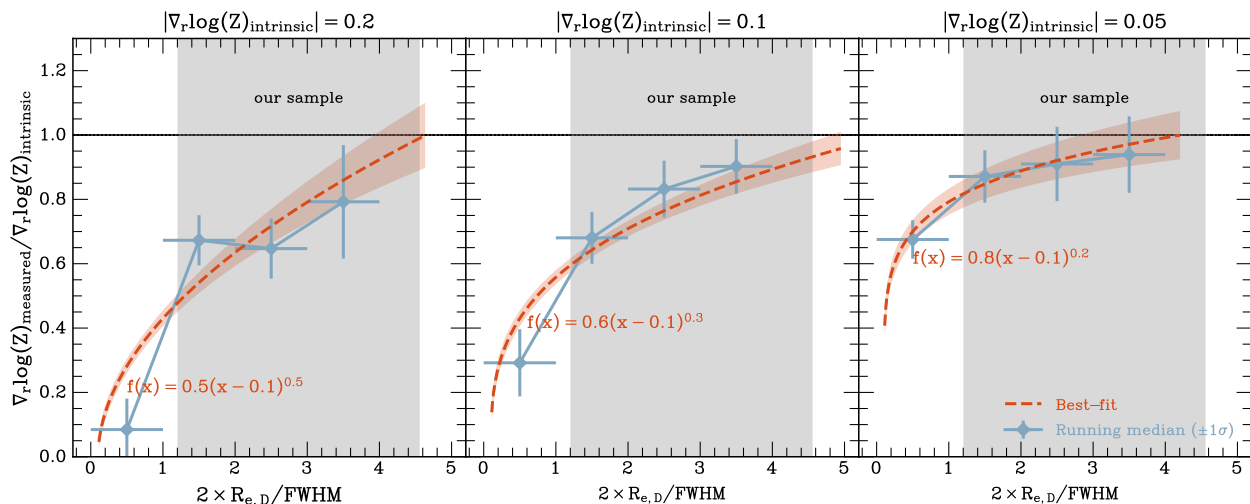


Fig. 8: Ratio of the measured ($\nabla_r \log(Z)_{\text{measured}}$) vs. intrinsic ($\nabla_r \log(Z)_{\text{intrinsic}}$) metallicity gradient for a set of mock exponential disk models imprinted with a linear intrinsic gradient ranging from $\pm[0.05, 0.10, 0.20]$ dex kpc^{-1} (from right to left) as a function of $2 \times R_{e,\text{disk}}/\text{beam}_{\text{FWHM}}$. The orange dashed line denotes the best-fit polynomials through the distribution, with the functional form annotated. The light blue curve shows the running median through the same distribution. The vertical grey band indicates the range of $2 \times R_{e,\text{disk}}/\text{beam}_{\text{FWHM}}$ spanned by our data. We infer the correction factor by inverting the orange curves for different intrinsic gradients. The median $2 \times R_{e,\text{disk}}/\text{beam}_{\text{FWHM}}$ of our sample is 2.5.

Table 4: Parameters of mock data cubes at $z = 5$

Parameter	(Range of) Value
$\log(M_{\text{bary}}/M_{\odot})$	10.5
$R_{e,\text{disk}}$ (kpc)	2
σ_0 (km s^{-1})	80
σ_{LSF} (km s^{-1}) ^a	125
$\text{beam}_{\text{FWHM}}$	0'1–1'0
$2 \times R_{e,\text{disk}}/\text{beam}_{\text{FWHM}}$	0.6–6.4
S/N ^b	20–40
Pixel scale	0'05
$\nabla_r \log(Z)$ (dex kpc^{-1})	$[-0.20, +0.20]$
Inclination	20°

Notes. ^(a) In σ . ^(b) Average per-pixel S/N within an effective radius of the channel of the brightest line.

already been de-reddened. The light profile follows that of an exponential disk (Sérsic index = 1). The central metallicity Z_0 is chosen such that over the extent of the profile, $\log_{10} Z(r)$ falls within the valid range of R3, O32 and Ne3O2 as listed in Table 2.

The cubes are convolved with a PSF of varying sizes, such that the galaxy extent in diameter ($2 \times R_{e,\text{disk}}$) is covered by 0.6 to 6.4 beams in FWHM ($\text{beam}_{\text{FWHM}}$). The intrinsic effective radii of our galaxies range from 0'11 to 0'40, measured from *imfit* modelling of the F444W photometry (Lee et al. 2025a).⁹ We assume that the line emission follows the stellar light traced by the F444W continuum. Therefore, for our data, $2 \times R_{e,\text{disk}}/\text{beam}_{\text{FWHM}} \sim 2.5$ (median), with a range of ~ 1.2 –4.5.

The cubes are also convolved with a LSF kernel of size (in σ) 125 km s^{-1} ($1.28 \times 10^{-3} \mu\text{m}$), corresponding approximately to the spectral resolution of the $R \sim 1000$ NIRSpec IFU at the observed wavelength of [O III] ($\sim 3 \mu\text{m}$). The channel width is fixed at 106 km s^{-1} . The pixel scale is set to 0'05 pix^{-1} (compared to 0'1 pix^{-1} in the NIRSpec data) to sample the smaller PSF in

⁹ For CRISTAL-10a-E, in which F444W is unavailable, we measure the effective radius from the H α line map.

some of the mock cubes. This finer pixel scale is chosen to avoid the undesirable situation where the pixel size is larger than the smallest beam FWHM. Since the axis ratios of the actual PSF $\gtrsim 0.9$, the PSF shape of the mock cubes is set to be circular. To simulate a range of S/N covered by our data and slightly beyond to recover trends, we add Gaussian noise to the data cubes, resulting in average per-pixel S/N values of 20 to 100 within the effective radius of the brightest channel of the [O III] $\lambda 5007$ emission line. Such definition of S/N means that the [Ne III] $\lambda 3869$ line may be undetected in some of the mock cubes, particularly those with high metallicity. In such cases, we exclude the use of the Ne3O2 diagnostic to recover the metallicity, as in our treatment of the actual data.

We then repeat the spectral line fitting and derive the azimuthally-averaged metallicity gradients of the mock data cubes following the same procedure in Sect. 3 and Sect. 4, respectively. The resulting distributions of the recovered versus the intrinsic metallicity gradients as a function of $2 \times R_{e,\text{disk}}/\text{beam}_{\text{FWHM}}$ is shown in Fig. 8.

As expected, we find a positive correlation between the number of beams covering a galaxy and the accuracy of the recovered intrinsic metallicity gradient. Additionally, there is a secondary dependence on the intrinsic metallicity gradient, as evidenced by the shallower correlation when the intrinsic gradient is 0.05 dex kpc^{-1} in absolute value, compared to 0.2 dex kpc^{-1} . This suggests that a shallower intrinsic gradient is less affected by beam smearing, consistent with the findings of Wuyts et al. (2016a). We do not observe a substantial difference in the correlation between the sign (negative vs. positive) of the gradients for a fixed magnitude. Furthermore, we find no strong dependence on S/N, which only affects the uncertainties and scatter, which is also reported by Wuyts et al. (2016a) and Gillman et al. (2021).

To quantify the correlation between the measured and intrinsic metallicity gradients, we fit a polynomial to the relationship between $\nabla_r \log(Z)_{\text{measured}}/\nabla_r \log(Z)_{\text{intrinsic}}$ and $2 \times R_{e,\text{disk}}/\text{beam}_{\text{FWHM}}$. The resulting fit is a reasonably good match to the running medians of the distribution, as shown in Fig. 8.

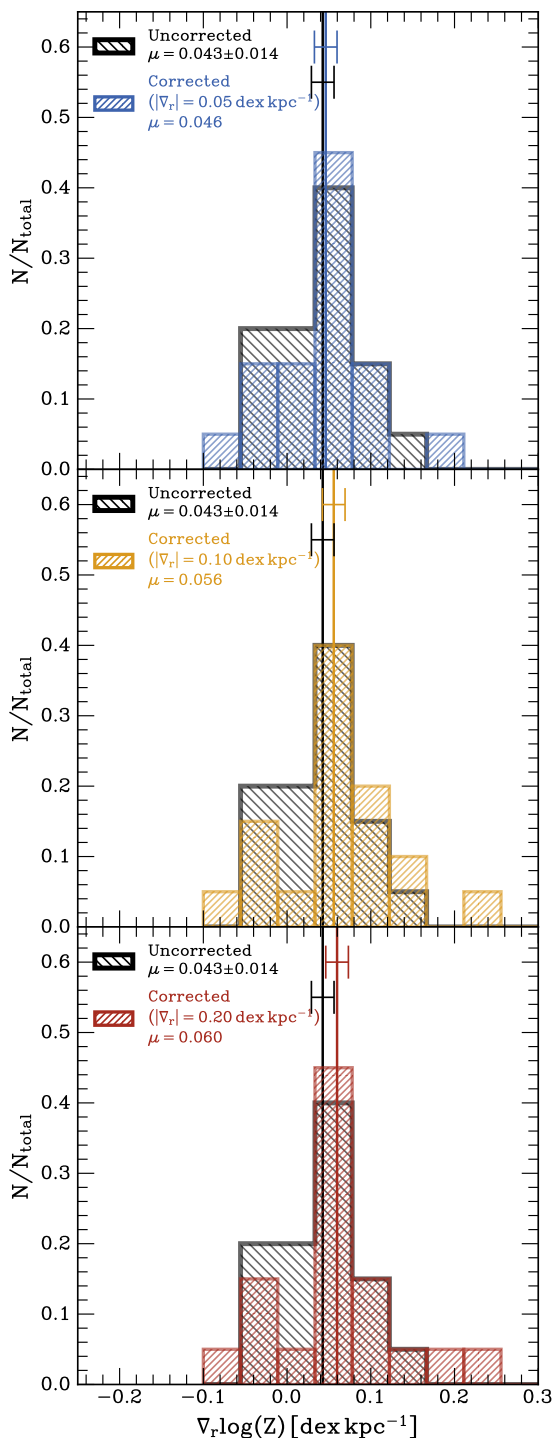


Fig. 9: Distributions of the observed metallicity gradients, as well as the corrected gradients obtained by applying correction factors derived from correction curves that assume different intrinsic metallicity gradients presented in Fig. 8. The error of the mean of the gradients is indicated by the horizontal error bar. Note that the error of the mean will not change after beam-smearing correction is applied.

We can then invert the best-fit polynomials to derive a ‘correction factor’ based on the $2 \times R_{e,\text{disk}}/\text{beam}_{\text{FWHM}}$ ratio of an individual galaxy. Since the correction factor also depends on the unknown intrinsic metallicity gradient, we report the corrected gradients in Table E.3 for the range of $|\nabla_r \log(Z)_{\text{intrinsic}}| = [0.05, 0.2]$

that we have examined. For our data, the correction factors as we defined, $\nabla_r \log(Z)_{\text{measured}}/\nabla_r \log(Z)_{\text{intrinsic}}$, for $|\nabla_r \log(Z)_{\text{intrinsic}}| = [0.05, 0.10, 0.20]$ range across $[0.8, 1.0]$, $[0.6, 1.0]$ and $[0.5, 1.0]$, respectively. It is an interesting ancillary finding that, regardless of the intrinsic steepness of the gradients, the correction factors all asymptotically approach unity when the ratio of $2 \times R_{e,\text{disk}}/\text{beam}_{\text{FWHM}}$ reaches ~ 5 . In other words, one should aim for an angular resolution of this order to determine the intrinsic gradient that is not compromised too much by beam smearing.

After applying these correction factors, we find that the corrected metallicities remain largely consistent with a flat gradient, as found previously in Sect. 4, with a maximum correction of up to 20% (mean $\sim 10\%$) correction needed. For the 16/20 galaxies that exhibit positive metallicity gradients, applying the correction factors derived from an intrinsic gradient of $|\nabla_r \log(Z)_{\text{intrinsic}}| = 0.05 \text{ dex kpc}^{-1}$, we find that none of the galaxies have a metallicity gradient of $\nabla_r \log(Z) > +0.05 \text{ dex kpc}^{-1}$ at 3σ level, and only three galaxies (CRISTAL-01a, 07a, and 07b) have gradients at 1σ , consistent with the uncorrected results presented in Sect. 4. Even when applying the most extreme correction, assuming an intrinsic gradient of $|\nabla_r \log(Z)_{\text{intrinsic}}| = 0.2$, none of the galaxies have a metallicity gradient of $\nabla_r \log(Z) > +0.2 \text{ dex kpc}^{-1}$. For the 4/20 galaxies that exhibit negative metallicity gradients, their gradients remain consistent with a strictly flat metallicity gradient ($\nabla_r \log(Z) = 0 \text{ dex kpc}^{-1}$) within their 1σ uncertainty, regardless of the assumed intrinsic gradient. Fig. 9 presents the distributions of the corrected metallicity gradients, along with their mean values and the error of the mean, assuming different intrinsic gradients.

The investigation presented here demonstrates that, regardless of sign, the intrinsic metallicity gradients are unlikely to be extreme. This finding suggests that the intrinsic metallicity gradients of these galaxies are likely to be flat, rather than being solely an artefact of observational effects such as beam smearing.

Nevertheless, we note that our first-order beam-smearing correction has several caveats. First, we assume a smooth linear gradient when imprinting the mock data cubes, but observations of nearby galaxies have shown that their metallicity gradients may not be strictly linear. Instead, many local disks exhibit a double-linear slope within $\sim 2R_e$ (from Martin & Roy 1995 to more recent IFU studies Sánchez-Menguiano et al. 2018; Easeman et al. 2022; Cardoso et al. 2025), but evidence at higher redshifts is still lacking. Furthermore, high- z disks are often characterised by actively star-forming clumps, which could introduce local metallicity irregularities (e.g. Wang et al. 2017; Estrada-Carpenter et al. 2025; Sok et al. 2025), and light-weighting effects distinct from those for our assumed exponential disk profiles, in addition to other mechanisms that would give rise to local variations as discussed in Sect. 5.3, that a smooth gradient as a function of galactic radius only cannot capture.

7. Summary

In this work, we analysed the gas-phase oxygen abundance (metallicity) gradients of 20 MS SFGs at $4 < z < 6$ using JWST/NIRSpec IFU at $\sim 1 \text{ kpc}$ resolution. We measured the metallicity at each radial position using the strong-line method with T_e -based metallicity calibration (Sanders et al. 2025), leveraging the multiple optical emission lines available, from $[\text{O II}] \lambda\lambda 3726, 29$ to $[\text{S II}] \lambda\lambda 6716, 33$. We find the metallicity gradients across the sample are consistent with a flat gradient, with only three galaxies showing a gradient $> 0.05 \text{ dex kpc}^{-1}$ at only 1σ level (Sect. 4). We do not find a significant systematic offset

in the metallicity gradients inferred from different line diagnostics and the Bayesian approach could tighten the overall constraint on the metallicity (Sect. 4). We then examined the correlations between the metallicity gradient, kinematic properties, and other physical properties. We find the following:

1. By combining our disk sample with literature data, our study effectively increases the number of available samples at $3 \leq z \leq 8$ by 50% within the comparable mass range. The combined data set reveals a shallow yet statistically significant negative relationship between metallicity gradients and V_{rot}/σ_0 , but not with σ_0 . This trend is consistent with the reported cosmic evolution of metallicity gradients, which become progressively more negative from early to recent epochs (Fujimoto et al. 2025, and references therein). Fundamentally, our results suggest that the dynamical maturity of a galaxy disk, as indicated by V_{rot}/σ , plays a crucial role in shaping the radial metallicity gradients (Sect. 5.1).
2. There is no strong distinction between disks and non-disks; this could be due to the frequent accretion events and efficient gas transport at $z \sim 5$ as implied from their high gas fraction (Sect. 5.2).
3. The majority of our galaxies do not exhibit significant azimuthal variations, which may be attributed to the efficient azimuthal mixing in turbulent disks. However, we also acknowledge the potential observational limitations in resolving the physical scales of structures, such as clumps and spirals, that could potentially drive local metallicity variations (Sect. 5.3).
4. There is no statistically significant correlation with M_* , and only a marginal positive trend with sSFR, even when combining with literature samples at $z > 3$ of wider range in M_* and sSFR (Sect. 5.4).
5. Applying a beam-smearing correction to our sample, using correction factors derived from a large suite of mock galaxies that mimic the observational sample, indicates that beam smearing can account for a maximum of 20% flattening, and typically only 10%. Given the uncertainties, we rule out very steep metallicity gradients in the sample, regardless of sign (Sect. 6).

Overall, the lack of a strong correlation between the metallicity gradients and the kinematic nature and global physical properties, especially the former, may be due to the limited dynamic range of the sample and the substantial scatter in the empirical data. Consequently, this only allows the identification of the steepest trends, while shallower trends, such as those presented here, will require much larger statistics to constrain more robustly. Our study, together with the two other works by Fujimoto et al. (2025) and Faisst et al. (2026), nevertheless provides a homogeneously selected set of MS SFGs sample available at $4 < z < 6$ that allows for comparison with gas kinematics properties.

Ideally, future studies should aim at even higher spatial resolution to examine the local metallicity variations on smaller physical scales than resolvable by JWST \lesssim kpc. Gravitational lensing can alleviate some observational limitations, yet strong lensing events are intrinsically rare, especially for sources at $z > 4$, so assembling a statistically significant sample to study at population-level remains challenging. The next-generation IFU, HARMONI, to be equipped on the Extremely Large Telescope (ELT), will offer a significant improvement in capabilities for study at $4 < z < 6$. With a linear spatial resolution ~ 6 times better and at least five-fold higher spectral resolution, HARMONI will

enable the study of local metallicity variations at physical scales of < 100 pc, although this will be restricted to rest-frame UV lines blueward of [Ne III] $\lambda 3869$ and [O II] $\lambda \lambda 3726, 29$ at $z \sim 5$ due to atmospheric transmission, which will require additional empirical calibrations for metallicity inference.

Acknowledgements. We thank the anonymous referee for the careful reading and constructive comments, which have improved the clarity of the manuscript. We acknowledge Michele Perna and Francesco D’Eugenio for their work in developing reduction scripts for NIRSpec IFU data. N.M.F.S., J.C. and G.T. acknowledge financial support from the European Research Council (ERC) Advanced Grant under the European Union’s (EU’s) Horizon Europe research and innovation programme (grant agreement AdG GALPHYS, No. 101055023). H.Ü. acknowledges funding by the EU (ERC APEX, 101164796). Views and opinions expressed are, however, those of the author(s) only and do not necessarily reflect those of the EU or the ERC. Neither the EU nor the granting authority can be held responsible for them. R.H.-C. thanks the Max Planck Society for support under the Partner Group project ‘The Baryon Cycle in Galaxies’ between the Max Planck for Extraterrestrial Physics and the Universidad de Concepción. T.N. acknowledges support from the Deutsche Forschungsgemeinschaft (DFG, German Research Foundation) under Germany’s Excellence Strategy – EXC - 2094 - 390783311 from the DFG Cluster of Excellence ‘ORIGINS’. M.A. is supported by FONDECYT grant number 1252054, and gratefully acknowledges support from ANID Basal Project FB210003. M.A. and J.M. gratefully acknowledges support from ANID MILENIO NCN2024_112. M.B. acknowledges support from the ANID BASAL project FB210003. This work was supported by the French government through the France 2030 investment plan managed by the National Research Agency (ANR), as part of the Initiative of Excellence of Université Côte d’Azur under reference number ANR-15-IDEX-01. E.d.C. acknowledges support from the Australian Research Council (project DP240100589). R.L.D. is supported by the Australian Research Council through the Discovery Early Career Researcher Award (DECRA) Fellowship DE240100136 funded by the Australian Government. D.R. gratefully acknowledges support from the Collaborative Research Center 1601 (SFB 1601 subprojects C1, C2, C3, and C6) funded by the Deutsche Forschungsgemeinschaft (DFG) – 500700252. M.R. acknowledges support from project PID2023-150178NB-I00 financed by MCIU/AEI/10.13039/501100011033, and by FEDER, UE. A.N acknowledges support from the Narodowe Centrum Nauki (NCN), Poland, through the SONATA BIS grant UMO-2020/38/E/ST9/00077. D.B.S. gratefully acknowledges support from NSF Grant 2407752. W.W. also acknowledges support associated with program JWST-GO-03950. These observations are associated with programs JWST-GO-03045 and JWST-GO-04265. Support for program JWST-GO-03045 was provided by NASA through a grant from the Space Telescope Science Institute, which is operated by the Association of Universities for Research in Astronomy, Inc., under NASA contract NAS 5-03127. This work is based in part on observations made with the NASA/ESA/CSA James Webb Space Telescope. The data were obtained from the Mikulski Archive for Space Telescopes (MAST) at the Space Telescope Science Institute, which is operated by the Association of Universities for Research in Astronomy, Inc., under NASA contract NAS 5-03127. The specific observations analysed can be accessed via [10.17909/cqds-qc81](https://doi.org/10.17909/cqds-qc81). This work made use of the following Python packages: Astropy (Astropy Collaboration et al. 2022), corner (Foreman-Mackey 2016), DYSMALPy (Davies et al. 2004b,a; Cresci et al. 2009; Davies et al. 2011; Wuyts et al. 2016b; Lang et al. 2017; Price et al. 2021; Lee et al. 2025b), emcee (Foreman-Mackey et al. 2013), Matplotlib (Hunter 2007), Numpy (Harris et al. 2020), pymccorrelation (Curran 2014; Privon et al. 2020), and Scipy (Virtanen et al. 2020).

References

- Acharyya, A., Krumholz, M. R., Federrath, C., et al. 2020, *MNRAS*, **495**, 3819
 Acharyya, A., Peeples, M. S., Tumlinson, J., et al. 2025, *ApJ*, **979**, 129
 Alloin, D., Edmunds, M. G., Lindblad, P. O., & Pagel, B. E. J. 1981, *A&A*, **101**, 377
 Arribas, S., Perna, M., Rodríguez Del Pino, B., et al. 2024, *A&A*, **688**, A146
 Asplund, M., Grevesse, N., Sauval, A. J., & Scott, P. 2009, *ARA&A*, **47**, 481
 Astropy Collaboration, Price-Whelan, A. M., Lim, P. L., et al. 2022, *ApJ*, **935**, 167
 Baldwin, J. A., Phillips, M. M., & Terlevich, R. 1981, *PASP*, **93**, 5
 Barišić, I., Jones, T., Mortensen, K., et al. 2025, *ApJ*, **983**, 139
 Behrendt, M., Burkert, A., & Schartmann, M. 2015, *MNRAS*, **448**, 1007
 Belfiore, F., Santoro, F., Groves, B., et al. 2022, *A&A*, **659**, A26
 Bellardini, M. A., Wetzel, A., Loebman, S. R., et al. 2021, *MNRAS*, **505**, 4586
 Béthermin, M., Fudamoto, Y., Ginolfi, M., et al. 2020, *A&A*, **643**, A2
 Bian, F., Kewley, L. J., & Dopita, M. A. 2018, *ApJ*, **859**, 175
 Birkin, J. E., Hutchison, T. A., Welch, B., et al. 2023, *ApJ*, **958**, 64

- Birkin, J. E., Spilker, J. S., Herrera-Camus, R., et al. 2025, *ApJ*, 985, 243
- Bournaud, F., Dekel, A., Teyssier, R., et al. 2011, *ApJ*, 741, L33
- Bournaud, F., Elmegreen, B. G., & Elmegreen, D. M. 2007, *ApJ*, 670, 237
- Bresolin, F., Fernández-Arenas, D., Rousseau-Nepton, L., et al. 2025, *MNRAS*, 539, 755
- Calzetti, D., Armus, L., Bohlin, R. C., et al. 2000, *ApJ*, 533, 682
- Cappellari, M. 2023, *MNRAS*, 526, 3273
- Cardoso, A. F. S., Cavichia, O., Mollá, M., & Sánchez-Menguiano, L. 2025, *ApJ*, 980, 45
- Carniani, S., Arribas, S., Bunker, A., et al. 2021, Galaxy assembly at $z > 6$: unraveling the origin of the spatial offset between the UV and FIR emission, JWST Proposal. Cycle 1, ID. #1893
- Carton, D., Brinchmann, J., Contini, T., et al. 2018, *MNRAS*, 478, 4293
- Ceverino, D., Mandelker, N., Snyder, G. F., et al. 2023, *MNRAS*, 522, 3912
- Ceverino, D., Sánchez Almeida, J., Muñoz Tuñón, C., et al. 2016, *MNRAS*, 457, 2605
- Chabrier, G. 2003, *PASP*, 115, 763
- Cheng, Y., Gialvalisco, M., Simons, R. C., et al. 2024, *ApJ*, 964, 94
- Chevance, M., Kruijssen, J. M. D., Hygate, A. P. S., et al. 2020, *MNRAS*, 493, 2872
- Chiappini, C., Matteucci, F., & Romano, D. 2001, *ApJ*, 554, 1044
- Clayssens, A., Adamo, A., Messa, M., et al. 2025, *MNRAS*, 537, 2535
- Clark, P. C., Glover, S. C. O., Ragan, S. E., & Duarte-Cabral, A. 2019, *MNRAS*, 486, 4622
- Cresci, G., Hicks, E. K. S., Genzel, R., et al. 2009, *ApJ*, 697, 115
- Cresci, G., Mannucci, F., Maiolino, R., et al. 2010, *Nature*, 467, 811
- Croxall, K. V., Pogge, R. W., Berg, D. A., Skillman, E. D., & Moustakas, J. 2015, *ApJ*, 808, 42
- Curran, P. A. 2014, *arXiv e-prints*, arXiv:1411.3816
- Curti, M., Cresci, G., Mannucci, F., et al. 2017, *MNRAS*, 465, 1384
- Curti, M., Maiolino, R., Cirasuolo, M., et al. 2020a, *MNRAS*, 492, 821
- Curti, M., Mannucci, F., Cresci, G., & Maiolino, R. 2020b, *MNRAS*, 491, 944
- Davies, R., Förster Schreiber, N. M., Cresci, G., et al. 2011, *ApJ*, 741, 69
- Davies, R. I., Tacconi, L. J., & Genzel, R. 2004a, *ApJ*, 613, 781
- Davies, R. I., Tacconi, L. J., & Genzel, R. 2004b, *ApJ*, 602, 148
- Dekel, A., Birnboim, Y., Engel, G., et al. 2009, *Nature*, 457, 451
- Dekel, A., Mandelker, N., Bournaud, F., et al. 2022, *MNRAS*, 511, 316
- D'Eugenio, F., Pérez-González, P. G., Maiolino, R., et al. 2024, *Nature Astronomy*, 8, 1443
- Di Teodoro, E. M., Grillo, C., Fraternali, F., et al. 2018, *MNRAS*, 476, 804
- Dopita, M. A. & Sutherland, R. S. 1995, *ApJ*, 455, 468
- Easeman, B., Schady, P., Wuyts, S., & Yates, R. M. 2022, *MNRAS*, 511, 371
- Epinat, B., Tasca, L., Amram, P., et al. 2012, *A&A*, 539, A92
- Estrada-Carpenter, V., Sawicki, M., Abraham, R., et al. 2025, *ApJ*, 991, 188
- Faisst, A. L., Fudamoto, Y., Oesch, P. A., et al. 2020, *MNRAS*, 498, 4192
- Faisst, A. L., Fujimoto, S., Tsujita, A., et al. 2026, *ApJS*, 282, 19
- Faisst, A. L., Liu, L.-J., Dubois, Y., et al. 2025, *arXiv e-prints*, arXiv:2510.16106
- Fasano, G. & Franceschini, A. 1987, *MNRAS*, 225, 155
- Fitzpatrick, E. L. & Massa, D. 2007, *ApJ*, 663, 320
- Foreman-Mackey, D. 2016, *The Journal of Open Source Software*, 1, 24
- Foreman-Mackey, D., Hogg, D. W., Lang, D., & Goodman, J. 2013, *PASP*, 125, 306
- Förster Schreiber, N. M., Genzel, R., Lehnert, M. D., et al. 2006, *ApJ*, 645, 1062
- Förster Schreiber, N. M., Renzini, A., Mancini, C., et al. 2018, *ApJS*, 238, 21
- Förster Schreiber, N. M. & Wuyts, S. 2020, *ARA&A*, 58, 661
- Fujimoto, S., Faisst, A. L., Tsujita, A., et al. 2025, *ApJ*, submitted
- Fujimoto, S., Silverman, J. D., Bethermin, M., et al. 2020, *ApJ*, 900, 1
- Garcia, A. M., Torrey, P., Bhagwat, A., et al. 2025, *ApJ*, 989, 147
- Genzel, R., Jolly, J. B., Liu, D., et al. 2023, *ApJ*, 957, 48
- Genzel, R., Newman, S., Jones, T., et al. 2011, *ApJ*, 733, 101
- Gibson, B. K., Pilkington, K., Brook, C. B., Stinson, G. S., & Bailin, J. 2013, *A&A*, 554, A47
- Gillman, S., Puglisi, A., Dudzevičiūtė, U., et al. 2022, *MNRAS*, 512, 3480
- Gillman, S., Tiley, A. L., Swinbank, A. M., et al. 2021, *MNRAS*, 500, 4229
- Girard, M., Dessauges-Zavadsky, M., Schaerer, D., et al. 2018, *A&A*, 613, A72
- Girard, M., Mason, C. A., Fontana, A., et al. 2020, *MNRAS*, 497, 173
- Gnerucci, A., Marconi, A., Cresci, G., et al. 2011, *A&A*, 528, A88
- Goldbaum, N. J., Krumholz, M. R., & Forbes, J. C. 2016, *ApJ*, 827, 28
- Grasha, K., Chen, Q. H., Battistini, A. J., et al. 2022, *ApJ*, 929, 118
- Harris, C. R., Millman, K. J., van der Walt, S. J., et al. 2020, *Nature*, 585, 357
- Harrison, C. M., Johnson, H. L., Swinbank, A. M., et al. 2017, *MNRAS*, 467, 1965
- Hemler, Z. S., Torrey, P., Qi, J., et al. 2021, *MNRAS*, 506, 3024
- Herrera-Camus, R., González-López, J., Förster Schreiber, N., et al. 2025, *A&A*, 699, A80
- Hirstenstein, J., Jones, T., Wang, X., et al. 2019, *ApJ*, 880, 54
- Ho, I. T., Kudritzki, R.-P., Kewley, L. J., et al. 2015, *MNRAS*, 448, 2030
- Huang, S., Kawabe, R., Umehata, H., et al. 2025, *Nature*, 641, 861
- Hunter, J. D. 2007, *Computing in Science and Engineering*, 9, 90
- Ibrahim, D. & Kobayashi, C. 2025, *arXiv e-prints*, arXiv:2501.11209
- Ikeda, R., Tadaki, K.-i., Mitsuhashi, I., et al. 2025, *A&A*, 693, A237
- Jiménez-Andrade, E. F., Cantalupo, S., Magnelli, B., et al. 2023, *MNRAS*, 521, 2326
- Johnson, H. L., Harrison, C. M., Swinbank, A. M., et al. 2018, *MNRAS*, 474, 5076
- Jones, G. C., Bunker, A. J., Telikova, K., et al. 2025, *MNRAS*, 540, 3311
- Jones, G. C., Vergani, D., Romano, M., et al. 2021, *MNRAS*, 507, 3540
- Jones, T., Ellis, R. S., Richard, J., & Jullo, E. 2013, *ApJ*, 765, 48
- Jones, T., Wang, X., Schmidt, K. B., et al. 2015, *AJ*, 149, 107
- Ju, M., Wang, X., Jones, T., et al. 2025, *ApJ*, 978, L39
- Kalita, B. S., Silverman, J. D., Daddi, E., et al. 2025, *MNRAS*, 537, 402
- Kewley, L. J. & Ellison, S. L. 2008, *ApJ*, 681, 1183
- Kewley, L. J., Nicholls, D. C., & Sutherland, R. S. 2019, *ARA&A*, 57, 511
- Kewley, L. J., Rupke, D., Zahid, H. J., Geller, M. J., & Barton, E. J. 2010, *ApJ*, 721, L48
- Khoperskov, S., Sivkova, E., Saburova, A., et al. 2023, *A&A*, 671, A56
- Kreckel, K., Ho, I. T., Blanc, G. A., et al. 2020, *MNRAS*, 499, 193
- Lang, P., Förster Schreiber, N. M., Genzel, R., et al. 2017, *ApJ*, 840, 92
- Le Fèvre, O., Béthermin, M., Faisst, A., et al. 2020, *A&A*, 643, A1
- Lee, L. L., Förster Schreiber, N. M., Herrera-Camus, R., et al. 2025a, *A&A*, 701, A260
- Lee, L. L., Förster Schreiber, N. M., Price, S. H., et al. 2025b, *ApJ*, 978, 14
- Leethochawalit, N., Jones, T. A., Ellis, R. S., et al. 2016, *ApJ*, 820, 84
- Li, J., Da Cunha, E., González-López, J., et al. 2024, *ApJ*, 976, 70
- Li, Z., Cai, Z., Wang, X., et al. 2025a, *arXiv e-prints*, arXiv:2506.12129
- Li, Z., Kakiichi, K., Christensen, L., et al. 2025b, *arXiv e-prints*, arXiv:2504.18616
- Li, Z., Wang, X., Cai, Z., et al. 2022, *ApJ*, 929, L8
- Lines, N. E. P., Bowler, R. A. A., Adams, N. J., et al. 2025, *MNRAS*, 539, 2685
- Liu, D., Förster Schreiber, N. M., Genzel, R., et al. 2023, *ApJ*, 942, 98
- Lyu, C., Wang, E., Zhang, H., et al. 2025, *ApJ*, 981, L6
- Ma, X., Hopkins, P. F., Wetzel, A. R., et al. 2017, *MNRAS*, 467, 2430
- Mainali, R., Stark, D. P., Jones, T., et al. 2023, *MNRAS*, 520, 4037
- Maiolino, R. & Mannucci, F. 2019, *A&A Rev.*, 27, 3
- Maiolino, R., Nagao, T., Grazian, A., et al. 2008, *A&A*, 488, 463
- Martin, P. & Roy, J.-R. 1994, *ApJ*, 424, 599
- Martin, P. & Roy, J.-R. 1995, *ApJ*, 445, 161
- Matteucci, F. & Francois, P. 1989, *MNRAS*, 239, 885
- Mazzolari, G., Übler, H., Maiolino, R., et al. 2024, *A&A*, 691, A345
- Mitsuhashi, I., Tadaki, K.-i., Ikeda, R., et al. 2024, *A&A*, 690, A197
- Molina, J., Ibar, E., Swinbank, A. M., et al. 2017, *MNRAS*, 466, 892
- Mollá, M., Díaz, Á. I., Cavichia, O., et al. 2019, *MNRAS*, 482, 3071
- Mott, A., Spitoni, E., & Matteucci, F. 2013, *MNRAS*, 435, 2918
- Nakajima, K., Ouchi, M., Xu, Y., et al. 2022, *ApJS*, 262, 3
- Newman, S. F., Shapiro Griffin, K., Genzel, R., et al. 2012, *ApJ*, 752, 111
- Oey, M. S., Meurer, G. R., Yelda, S., et al. 2007, *ApJ*, 661, 801
- Orr, M. E., Burkhardt, B., Wetzel, A., et al. 2023, *MNRAS*, 521, 3708
- Osterbrock, D. E. & Ferland, G. J. 2006, *Astrophysics of gaseous nebulae and active galactic nuclei*
- Pacifici, C., Iyer, K. G., Mobasher, B., et al. 2023, *ApJ*, 944, 141
- Parlanti, E., Carniani, S., Pallottini, A., et al. 2023, *A&A*, 673, A153
- Parlanti, E., Carniani, S., Venturi, G., et al. 2025a, *A&A*, 695, A6
- Parlanti, E., Tozzi, G., Förster Schreiber, N. M., et al. 2025b, *arXiv e-prints*, arXiv:2510.09820
- Pastras, S., Genzel, R., Tacconi, L. J., et al. 2025, *arXiv e-prints*, arXiv:2505.07925
- Patrício, V., Richard, J., Carton, D., et al. 2019, *MNRAS*, 489, 224
- Peacock, J. A. 1983, *MNRAS*, 202, 615
- Petit, A. C., Krumholz, M. R., Goldbaum, N. J., & Forbes, J. C. 2015, *MNRAS*, 449, 2588
- Pillepich, A., Nelson, D., Springel, V., et al. 2019, *MNRAS*, 490, 3196
- Poetrodjojo, H., D'Agostino, J. J., Groves, B., et al. 2019, *MNRAS*, 487, 79
- Posses, A. C., Aravena, M., González-López, J., et al. 2023, *A&A*, 669, A46
- Press, W. H., Teukolsky, S. A., Vetterling, W. T., & Flannery, B. P. 2007, *Numerical Recipes 3rd Edition: The Art of Scientific Computing*, 3rd edn. (USA: Cambridge University Press)
- Price, S. H., Shimizu, T. T., Genzel, R., et al. 2021, *ApJ*, 922, 143
- Privon, G. C., Ricci, C., Aalto, S., et al. 2020, *ApJ*, 893, 149
- Puglisi, A., Dudzevičiūtė, U., Swinbank, M., et al. 2023, *MNRAS*, 524, 2814
- Qeyrel, J., Contini, T., Kissler-Patig, M., et al. 2012, *A&A*, 539, A93
- Ren, W., Silverman, J. D., Faisst, A. L., et al. 2025, *arXiv e-prints*, arXiv:2509.02027
- Rizzo, F., Vegetti, S., Fraternali, F., Stacey, H. R., & Powell, D. 2021, *MNRAS*, 507, 3952
- Roman-Oliveira, F., Fraternali, F., & Rizzo, F. 2023, *MNRAS*, 521, 1045
- Romeo, A. B. & Falstad, N. 2013, *MNRAS*, 433, 1389
- Rowland, L. E., Hodge, J., Bouwens, R., et al. 2024, *MNRAS*, 535, 2068
- Rubet, M., Menéndez-Delmestre, K., Signorini Gonçalves, T., et al. 2025, *arXiv e-prints*, arXiv:2507.11804
- Rupke, D. S. N., Kewley, L. J., & Barnes, J. E. 2010a, *ApJ*, 710, L156

- Rupke, D. S. N., Kewley, L. J., & Chien, L. H. 2010b, *ApJ*, **723**, 1255
- Sánchez, S. F., Rosales-Ortega, F. F., Iglesias-Páramo, J., et al. 2014, *A&A*, **563**, A49
- Sánchez-Menguiano, L., Sánchez, S. F., Pérez, I., et al. 2018, *A&A*, **609**, A119
- Sanders, R. L., Shapley, A. E., Topping, M. W., et al. 2025, *arXiv e-prints*, [arXiv:2508.10099](https://arxiv.org/abs/2508.10099)
- Sanders, R. L., Shapley, A. E., Topping, M. W., Reddy, N. A., & Brammer, G. B. 2024, *ApJ*, **962**, 24
- Sanders, R. L., Shapley, A. E., Zhang, K., & Yan, R. 2017, *ApJ*, **850**, 136
- Schlafly, E. F. & Finkbeiner, D. P. 2011, *ApJ*, **737**, 103
- Scholtz, J., Curti, M., D'Eugenio, F., et al. 2025, *MNRAS*, **539**, 2463
- Sen, P. K. 1968, *Journal of the American Statistical Association*, **63**, 1379
- Shapley, A. E., Sanders, R. L., Shao, P., et al. 2019, *ApJ*, **881**, L35
- Shapley, A. E., Sanders, R. L., Topping, M. W., et al. 2025, *ApJ*, **980**, 242
- Sharda, P., Krumholz, M. R., Wisnioski, E., et al. 2021a, *MNRAS*, **502**, 5935
- Sharda, P., Wisnioski, E., Krumholz, M. R., & Federrath, C. 2021b, *MNRAS*, **506**, 1295
- Sharon, C. E., Tagore, A. S., Baker, A. J., et al. 2019, *ApJ*, **879**, 52
- Shirazi, M. & Brinchmann, J. 2012, *MNRAS*, **421**, 1043
- Simons, R. C., Papovich, C., Momcheva, I., et al. 2021, *ApJ*, **923**, 203
- Sobral, D., Swinbank, A. M., Stott, J. P., et al. 2013, *ApJ*, **779**, 139
- Sok, V., Muzzin, A., Jablonka, P., et al. 2025, *ApJ*, **979**, 14
- Solimano, M., González-López, J., Aravena, M., et al. 2025, *A&A*, **693**, A70
- Solimano, M., González-López, J., Aravena, M., et al. 2024, *A&A*, **689**, A145
- Speagle, J. S., Steinhardt, C. L., Capak, P. L., & Silverman, J. D. 2014, *ApJS*, **214**, 15
- Spitoni, E., Cescutti, G., Minchev, I., et al. 2019, *A&A*, **628**, A38
- Spitoni, E. & Matteucci, F. 2011, *A&A*, **531**, A72
- Spitoni, E., Romano, D., Matteucci, F., & Ciotti, L. 2015, *ApJ*, **802**, 129
- Stanghellini, L., Magrini, L., Casasola, V., & Villaver, E. 2014, *A&A*, **567**, A88
- Stark, D. P., Swinbank, A. M., Ellis, R. S., et al. 2008, *Nature*, **455**, 775
- Storey, P. J. & Zeppen, C. J. 2000, *MNRAS*, **312**, 813
- Stott, J. P., Sobral, D., Swinbank, A. M., et al. 2014, *MNRAS*, **443**, 2695
- Sun, X., Wang, X., Ma, X., et al. 2025, *ApJ*, **986**, 179
- Swinbank, A. M., Smail, I., Sobral, D., et al. 2012a, *ApJ*, **760**, 130
- Swinbank, A. M., Sobral, D., Smail, I., et al. 2012b, *MNRAS*, **426**, 935
- Tacconi, L. J., Genzel, R., & Sternberg, A. 2020, *Annual Review of Astronomy and Astrophysics*, **58**, 157
- Taylor, P. & Kobayashi, C. 2017, *MNRAS*, **471**, 3856
- Tiley, A. L., Gillman, S., Cortese, L., et al. 2021, *MNRAS*, **506**, 323
- Tissera, P. B., Rosas-Guevara, Y., Sillero, E., et al. 2022, *MNRAS*, **511**, 1667
- Troncoso, P., Maiolino, R., Sommariva, V., et al. 2014, *A&A*, **563**, A58
- Tsukui, T. & Iguchi, S. 2021, *Science*, **372**, 1201
- Tsukui, T., Wisnioski, E., Bland-Hawthorn, J., & Freeman, K. 2024, *arXiv e-prints*, [arXiv:2409.15909](https://arxiv.org/abs/2409.15909)
- Übler, H., D'Eugenio, F., Perna, M., et al. 2024, *MNRAS*, **533**, 4287
- Übler, H., Genzel, R., Wisnioski, E., et al. 2019, *ApJ*, **880**, 48
- Übler, H., Naab, T., Oser, L., et al. 2014, *MNRAS*, **443**, 2092
- Vale Asari, N., Couto, G. S., Cid Fernandes, R., et al. 2019, *MNRAS*, **489**, 4721
- Vallini, L., Gallerani, S., Ferrara, A., Pallottini, A., & Yue, B. 2015, *ApJ*, **813**, 36
- Vallini, L., Witstok, J., Sommovigo, L., et al. 2024, *MNRAS*, **527**, 10
- Venturi, G., Carniani, S., Parlanti, E., et al. 2024, *A&A*, **691**, A19
- Virtanen, P., Gommers, R., Oliphant, T. E., et al. 2020, *Nature Methods*, **17**, 261
- Vogt, F. P. A., Pérez, E., Dopita, M. A., Verdes-Montenegro, L., & Borthakur, S. 2017, *A&A*, **601**, A61
- Wang, B. & Silk, J. 1994, *ApJ*, **427**, 759
- Wang, H., Cañameras, R., Suyu, S. H., et al. 2024, *A&A*, **690**, A1
- Wang, X., Jones, T., Vulcani, B., et al. 2022, *ApJ*, **938**, L16
- Wang, X., Jones, T. A., Treu, T., et al. 2020, *ApJ*, **900**, 183
- Wang, X., Jones, T. A., Treu, T., et al. 2019, *ApJ*, **882**, 94
- Wang, X., Jones, T. A., Treu, T., et al. 2017, *ApJ*, **837**, 89
- Williams, T. G., Kreckel, K., Belfiore, F., et al. 2022, *MNRAS*, **509**, 1303
- Wisnioski, E., Mendel, J. T., Leaman, R., et al. 2025, *MNRAS*, **544**, 2777
- Wisiz, M. E., Masters, K. L., Daniel, K. J., Stark, D. V., & Belfiore, F. 2025, *ApJ*, **983**, 57
- Wolfire, M. G., McKee, C. F., Hollenbach, D., & Tielens, A. G. G. M. 2003, *ApJ*, **587**, 278
- Wuyts, E., Wisnioski, E., Fossati, M., et al. 2016a, *ApJ*, **827**, 74
- Wuyts, S., Förster Schreiber, N. M., Wisnioski, E., et al. 2016b, *ApJ*, **831**, 149
- Yang, C.-C. & Krumholz, M. 2012, *ApJ*, **758**, 48
- Yuan, T. T., Kewley, L. J., Swinbank, A. M., Richard, J., & Livermore, R. C. 2011, *ApJ*, **732**, L14
- Zaritsky, D., Kennicutt, Jr., R. C., & Huchra, J. P. 1994, *ApJ*, **420**, 87
- 1 Max-Planck-Institut für extraterrestrische Physik (MPE), Gießenbachstraße 1, 85748 Garching, Germany
- 2 David A. Dunlap Department of Astronomy and Astrophysics, University of Toronto, 50 St. George Street, Toronto, Ontario, M5S 3H4, Canada
- 3 Dunlap Institute for Astronomy and Astrophysics, 50 St. George Street, Toronto, Ontario, M5S 3H4, Canada
- 4 IPAC, California Institute of Technology, 1200 E. California Blvd. Pasadena, CA 91125, USA
- 5 Departamento de Astronomía, Universidad de Concepción, Barrio Universitario, Concepción, Chile
- 6 Millenium Nucleus for Galaxies (MINGAL), Concepción, Chile
- 7 Departments of Physics and Astronomy, University of California, Berkeley, CA 94720, USA
- 8 Osservatorio Astronomico di Padova, Vicolo dell'Osservatorio 5, Padova, I-35122, Italy
- 9 Department of Physics and Astronomy, University of Kentucky, 505 Rose Street, Lexington, KY 40506, USA
- 10 Research School of Astronomy and Astrophysics, Australian National University, Canberra, ACT 2611, Australia
- 11 Department of Physics, University of Bath, Claverton Down, Bath BA2 7AY, UK
- 12 Scuola Normale Superiore, Piazza dei Cavalieri 7, I-56126 Pisa, Italy
- 13 Kavli Institute for Cosmology, University of Cambridge, Madingley Road, Cambridge CB3 0HA, UK
- 14 Cavendish Laboratory, University of Cambridge, 19 JJ Thomson Avenue, Cambridge CB3 0HE, UK
- 15 Purple Mountain Observatory, Chinese Academy of Sciences, 10 Yuanhua Road, Nanjing 210023, China
- 16 Universitäts-Sternwarte Ludwig-Maximilians-Universität (USM), Scheinerstr. 1, München, D-81679, Germany
- 17 Space Telescope Science Institute, 3700 San Martin Drive, MD 21218, USA
- 18 Instituto de Estudios Astrofísicos, Facultad de Ingeniería y Ciencias, Universidad Diego Portales, Av. Ejército 441, Santiago, Chile
- 19 Millenium Nucleus for Galaxies (MINGAL), Santiago, Chile
- 20 Université Côte d'Azur, Observatoire de la Côte d'Azur, CNRS, Laboratoire Lagrange, 06000, Nice, France
- 21 Observatoire Astronomique de Strasbourg, UMR 7550, CNRS, Université de Strasbourg, F-67000 Strasbourg, France
- 22 International Centre for Radio Astronomy Research (ICRAR), The University of Western Australia, M468, 35 Stirling Highway, Crawley, WA 6009, Australia
- 23 Swinburne University, John St, Hawthorn, VIC, 3122, Australia
- 24 Sterrenkundig Observatorium, Ghent University, Krijgslaan 281 S9, B-9000 Ghent, Belgium
- 25 Department of Astronomy, University of Geneva, Chemin Pegasi 51, 1290 Versoix, Switzerland
- 26 Swinburne University, John St, Hawthorn, VIC, 3183, Australia
- 27 Cosmic Dawn Center (DAWN), Copenhagen, Denmark
- 28 DTU-Space, Elektrovej, Building 328, 2800 Kgs. Lyngby, Denmark
- 29 Università di Firenze, Dipartimento di Fisica e Astronomia, via G. Sansone 1, 50019 Sesto F.no, Firenze, Italy
- 30 Instituto de Física y Astronomía, Universidad de Valparaíso, Avda. Gran Bretaña 1111, Valparaíso, Chile
- 31 Millenium Nucleus for Galaxies (MINGAL), Avda. Gran Bretaña 1111, Valparaíso, Chile
- 32 Space Telescope Science Institute, 3700 San Martin Dr., Baltimore, MD 21218, USA
- 33 Max-Planck Institut für Astrophysik, Karl-Schwarzschild Straße 1, D-85748 Garching, Germany
- 34 Dept. Física Teórica y del Cosmos, Campus de Fuentenueva, Edificio Mecnas, Universidad de Granada, E-18071, Granada, Spain
- 35 Instituto Universitario Carlos I de Física Teórica y Computacional, Universidad de Granada, 18071, Granada, Spain
- 36 Institut für Astrophysik, Universität zu Köln, Zùlpicher Straße 77, D-50937 Köln, Germany

- ³⁷ Institute for Astronomy, University of Hawaii, 2680 Woodlawn Drive, Honolulu, HI 96822, USA
- ³⁸ Department of Physics and Astronomy and George P. and Cynthia Woods Mitchell Institute for Fundamental Physics and Astronomy, Texas A&M University, 4242 TAMU, College Station, TX 77843-4242, US
- ³⁹ INAF – Osservatorio di Astrofisica e Scienza dello Spazio di Bologna, Via Gobetti 93/3, 40129 Bologna, Italy
- ⁴⁰ National Centre for Nuclear Research, ul. Pasteura 7, 02-093 Warsaw, Poland
- ⁴¹ INAF – Osservatorio Astronomico d’Abruzzo, Via Maggini SNC, 64100 Teramo, Italy
- ⁴² Dipartimento di Fisica e Astronomia Galileo Galilei Università degli Studi di Padova, Vicolo dell’Osservatorio 3, 35122 Padova, Italy
- ⁴³ Institute of Astrophysics, Foundation for Research and Technology-Hellas (FORTH), Heraklion, 70013, Greece
- ⁴⁴ School of Sciences, European University Cyprus, Diogenes Street, Engomi 1516, Nicosia, Cyprus
- ⁴⁵ Department of Physics & Astronomy, University of California, Riverside, 900 University Ave., Riverside, CA 92521, USA
- ⁴⁶ Department of Astronomy, School of Science, SOKENDAI (The Graduate University for Advanced Studies), 2-21-1 Osawa, Mitaka, Tokyo 181-8588, Japan
- ⁴⁷ National Astronomical Observatory of Japan, 2-21-1 Osawa, Mitaka, Tokyo 181-8588, Japan
- ⁴⁸ Max-Planck-Institut für Radioastronomie, Auf dem Hügel 69, 53121 Bonn, Germany
- ⁴⁹ INAF – Osservatorio Astronomico di Padova, Vicolo dell’Osservatorio 5, I-35122 Padova, Italy
- ⁵⁰ School of Physics and Astronomy, Tel Aviv University, Tel Aviv 69978, Israel
- ⁵¹ Centre for Computational Astrophysics, Flatiron Institute, 162 5th Avenue, New York, NY 10010, USA

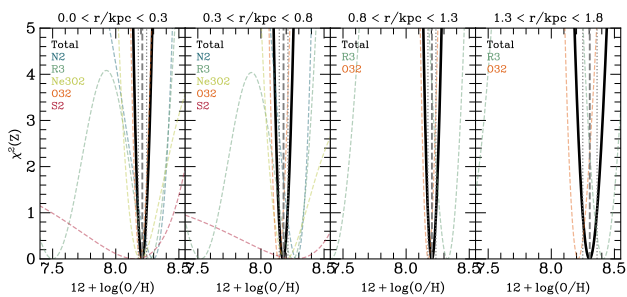


Fig. A.1: Example of the χ^2 landscape as a function of metallicity for CRISTAL-19 for each radial bin. The χ^2 values for each diagnostic are shown as coloured dashed lines, while the total χ^2 from the combined measurements is represented by a black thick curve. The 1σ confidence interval is indicated by two vertical dotted lines, and the best-fitting value is marked with a thick vertical grey dashed line.

Appendix A: Inferring metallicity via a Bayesian method

In Sect. 4, we describe how we derive metallicity using the various diagnostics in Table 2 using a Bayesian approach (our Method I). The χ^2 value is computed from the residuals between the observed line ratios and the values predicted by the calibration relations at a given metallicity, and we use the emcee ensemble sampler to map the posterior distribution. The metallicity that minimises χ^2 (equivalently, maximises the likelihood for flat priors) is taken as our best-fitting value. Fig. A.1 shows an example (CRISTAL-19) of the resulting χ^2 - $12 + \log(\text{O}/\text{H})$ curves, plotted for each diagnostic individually and in combination. The figure demonstrates the advantage of combining multiple diagnostics, which provides greater constraining power than any single diagnostic on its own.

Appendix B: Metallicity gradients inferred from each diagnostic

As discussed in Sect. 4, the line diagnostics we used are not all independent, which would underestimate the uncertainties of the best-fit gradients using the Bayesian approach (Method I). To better estimate the uncertainties and to examine the systematics associated with different line tracers, we alternatively infer the metallicities by simply inverting the calibration relations to find the solution given a line ratio, which we refer to as Method II in Sect. 4.

Table E.1 lists the metallicity gradients derived with Method II for each emission-line diagnostic. Figure E.2 compares these values with the gradients obtained using Method I. Overall, the two methods agree within 1σ uncertainties. The figure also demonstrates that gradients inferred from a single diagnostic carry relatively large uncertainties, whereas the Bayesian method adopted in Method I provides tighter constraints.

Appendix C: Literature sample

Table E.4 lists the references from which we compiled the metallicity gradient measurements, as well as kinematics results where available.

As noted in Sect. 5.1, the literature compilation is heterogeneous: the data were taken with a variety of instruments, span a

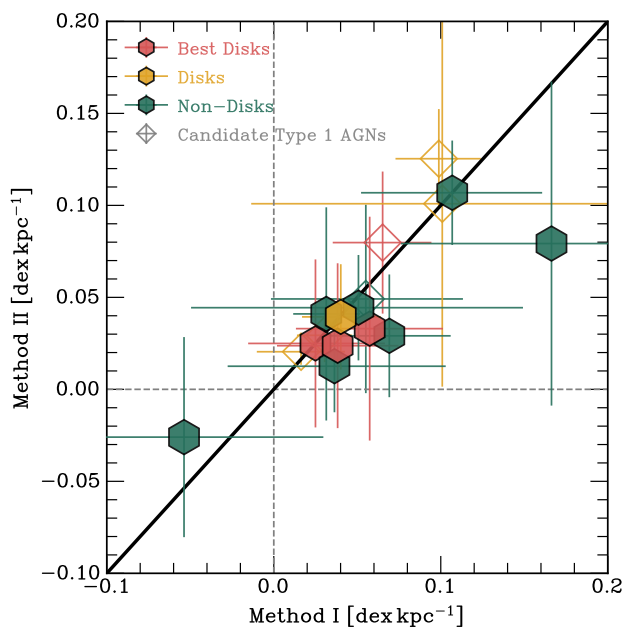


Fig. A.2: Comparison between the metallicity gradients inferred from the Bayesian method (‘All’) and the median from Method II (‘Median’). The disks and non-disks classified in Lee et al. (2025a) are shown in pink/yellow and green, respectively. The candidate Type-1 AGNs identified in Ren et al. (2025) are marked with the empty diamond symbol. CRISTAL-06b is not shown because only one diagnostic N2 is used for Method I.

wide range of spatial resolutions, and employ different metallicity diagnostics. While this diversity is not ideal, applying a stellar mass cut to select a subsample within the mass range of our sample results in a significantly reduced sample size: only 206 at cosmic noon and 35 galaxies beyond (see Fig. 4). Therefore, to maximise the statistics, we have chosen to retain the literature sample as is. Future work on a more unified sample selection would be highly valuable.

Fig. E.1 presents the stellar mass distribution of the final mass-matched sample at $z < 3$ and $z \geq 3$. The stellar mass distribution of the $z < 3$ sample is generally well-matched with our sample. However, the $z \geq 3$ sample skews towards $\log(M_*/M_\odot) \leq 9.4$, which is contributed mostly from $z > 6$ galaxies in this redshift range. These high-redshift galaxies are predominantly low-mass sources in the literature.

As pointed out in Sect. 5.1, our compilation does not attempt to homogenise the gas tracer nor the modelling methodologies used in the various studies. Whether the intrinsic velocity dispersion (σ_0) and the ratio V_{rot}/σ_0 differ systematically between ionised (e.g. $\text{H}\alpha$, $[\text{O III}]$) and molecular or neutral gas tracers at $z \geq 1$ is still uncertain, largely due to limited statistics from studies that have employed multiple tracers for the same object. Future work would benefit from comparing kinematics from multiple tracers for a consistent set of objects. For JWST-ALPINE-CRISTAL, D. Gomez-Espinoza et al. (in prep.) will present the kinematics of our sample as traced by ionised gas.

Appendix D: Azimuthally-binned metallicity gradients

To examine the azimuthal variation at a fixed radius, as discussed in Sect. 5.3, we binned the pixels within every azimuthal angle

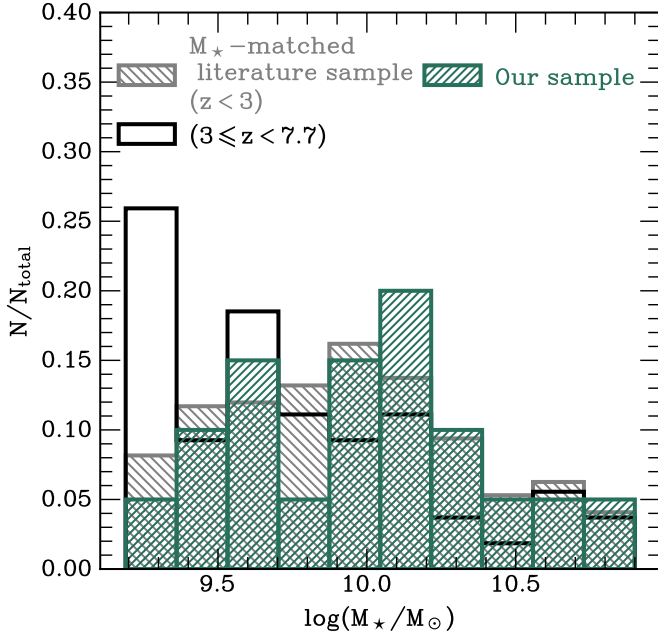


Fig. E.1: Distributions of stellar mass M_* for literature samples within the mass range of our sample ($z \geq 3$ in black, $z < 3$ in hatched grey). The M_* distribution of our sample is overlaid in hatched green. The peak at $\log(M_*/M_\odot) \lesssim 9.4$ for the $z \geq 3$ sample is primarily contributed by the sources at $z > 6$.

range of $\Delta\phi = 30^\circ$, where the azimuthal angle is defined as the acute angle difference from the morphological major axis. The resulting metallicity gradients for 11 galaxies for each azimuthal bin are summarised in Table E.2.

Appendix E: Beam smearing-corrected metallicity gradients

Table E.3 lists the metallicity gradients that are corrected for beam smearing, based on the correction curves derived in Sect. 6. Since the correction factors for a given angular resolution relative to galaxy size depend on the absolute intrinsic unknown gradients, we report the corrected values for a range of assumed intrinsic gradients that we have examined, i.e. $|\nabla_r \log(Z)| = [0.05, 0.10, 0.20]$.

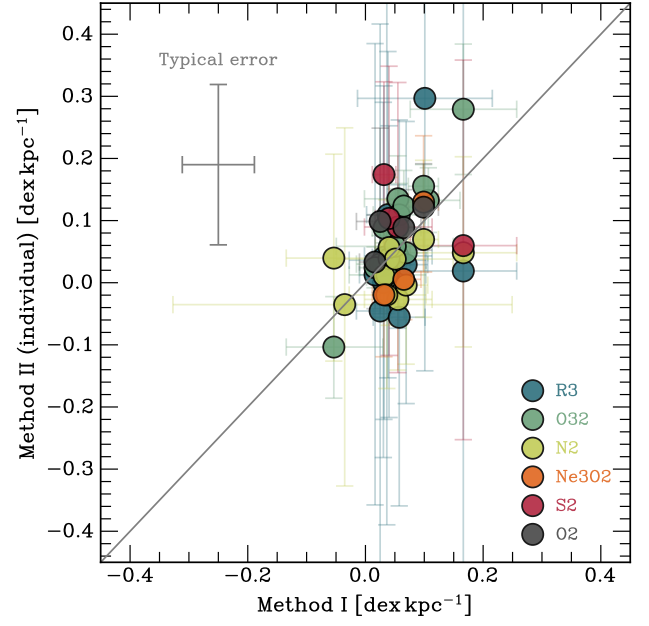


Fig. E.2: Comparison of the metallicity gradients derived from Method I and individual line diagnostics (Method II). The values are listed in Table E.1. The grey diagonal line is the line of equality. The typical uncertainty is shown at the upper left. The uncertainties associated with individual line diagnostics are large, but combining multiple line diagnostics with the Bayesian approach in Method I can tighten the overall constraints.

Table E.1: Metallicity gradients inferred from individual diagnostics.

ID	R3 (dex kpc ⁻¹)	O32 (dex kpc ⁻¹)	N2 (dex kpc ⁻¹)	Ne3O2 (dex kpc ⁻¹)	S2 (dex kpc ⁻¹)	O2 (dex kpc ⁻¹)
01a	...	0.133 ^{+0.052} _{-0.052}
02	0.000 ^{+0.290} _{-0.282}	0.028 ^{+0.027} _{-0.026}
03	...	0.123 ^{+0.057} _{-0.058}	...	0.005 ^{+0.068} _{-0.065}	...	0.089 ^{+0.061} _{-0.060}
04a	0.041 ^{+0.276} _{-0.261}	0.088 ^{+0.024} _{-0.024}	0.011 ^{+0.069} _{-0.068}	-0.020 ^{+0.107} _{-0.100}	0.174 ^{+0.149} _{-0.156}	...
05a	0.043 ^{+0.115} _{-0.116}	0.135 ^{+0.069} _{-0.073}	-0.027 ^{+0.114} _{-0.114}	...	0.090 ^{+0.233} _{-0.234}	...
06a	...	-0.104 ^{+0.081} _{-0.082}	0.040 ^{+0.167} _{-0.166}
06b	-0.035 ^{+0.285} _{-0.292}
07a	...	0.155 ^{+0.035} _{-0.037}	0.070 ^{+0.127} _{-0.125}	0.130 ^{+0.107} _{-0.113}	...	0.122 ^{+0.070} _{-0.069}
07b	0.019 ^{+0.512} _{-0.406}	0.279 ^{+0.105} _{-0.105}	0.048 ^{+0.155} _{-0.152}	...	0.060 ^{+0.299} _{-0.312}	...
09	0.297 ^{+0.406} _{-0.439}
10a-E	0.013 ^{+0.372} _{-0.370}	0.024 ^{+0.033} _{-0.032}	0.033 ^{+0.076} _{-0.075}
11	-0.046 ^{+0.462} _{-0.445}	0.030 ^{+0.046} _{-0.046}	0.099 ^{+0.150} _{-0.148}
13	0.029 ^{+0.230} _{-0.224}	0.048 ^{+0.036} _{-0.037}	-0.004 ^{+0.129} _{-0.127}
14	0.036 ^{+0.429} _{-0.426}	0.013 ^{+0.062} _{-0.062}	-0.020 ^{+0.153} _{-0.151}
15	-0.056 ^{+0.317} _{-0.304}	0.109 ^{+0.050} _{-0.052}
19	0.110 ^{+0.263} _{-0.263}	0.009 ^{+0.037} _{-0.037}
25	...	0.059 ^{+0.092} _{-0.093}	0.038 ^{+0.081} _{-0.081}
VC-7875	0.015 ^{+0.238} _{-0.232}	0.039 ^{+0.030} _{-0.031}	0.057 ^{+0.113} _{-0.125}	...	0.103 ^{+0.245} _{-0.221}	...

Notes. The outermost radius at which each diagnostic line is measured for each galaxy is annotated in Fig. 2. We only fit a gradient when there are more than two data points available for the diagnostic. Fig. E.2 shows a comparison between these gradients with that inferred from Method I.

Table E.2: Metallicity gradients of 11 galaxies in three azimuthal bins.

ID	[0°, 30°] ^a (dex kpc ⁻¹)	[30°, 60°] ^a (dex kpc ⁻¹)	[60°, 90°] ^a (dex kpc ⁻¹)
02	0.044 ^{+0.011} _{-0.012}	0.050 ^{+0.020} _{-0.020}	0.008 ^{+0.017} _{-0.016}
03	0.048 ^{+0.018} _{-0.018}	0.138 ^{+0.021} _{-0.020}	0.070 ^{+0.017} _{-0.018}
04a	0.043 ^{+0.010} _{-0.011}	0.073 ^{+0.023} _{-0.020}	0.052 ^{+0.023} _{-0.020}
11	0.006 ^{+0.015} _{-0.014}	0.020 ^{+0.012} _{-0.012}	0.051 ^{+0.022} _{-0.022}
13	-0.018 ^{+0.008} _{-0.008}	-0.011 ^{+0.011} _{-0.011}	-0.000 ^{+0.038} _{-0.037}
15	0.011 ^{+0.010} _{-0.010}	0.032 ^{+0.020} _{-0.019}	0.068 ^{+0.034} _{-0.035}
19	-0.041 ^{+0.020} _{-0.020}	0.019 ^{+0.039} _{-0.038}	0.049 ^{+0.022} _{-0.023}
20	-0.027 ^{+0.021} _{-0.022}	-0.015 ^{+0.038} _{-0.037}	-0.031 ^{+0.051} _{-0.053}
22a	-0.059 ^{+0.029} _{-0.030}	-0.040 ^{+0.019} _{-0.018}	0.013 ^{+0.022} _{-0.021}
25	-0.049 ^{+0.032} _{-0.031}	0.003 ^{+0.033} _{-0.032}	0.037 ^{+0.064} _{-0.058}
VC-7875	0.062 ^{+0.011} _{-0.011}	-0.020 ^{+0.015} _{-0.015}	-0.027 ^{+0.019} _{-0.019}

Notes. ^(a) The acute azimuthal angle difference from the major axis.

Table E.3: Metallicity gradients corrected for beam smearing.

ID	$\nabla_r \log(Z)$ ($ \nabla_r \log(Z) = 0.20$) (dex kpc ⁻¹)	$\nabla_r \log(Z)$ ($ \nabla_r \log(Z) = 0.10$) (dex kpc ⁻¹)	$\nabla_r \log(Z)$ ($ \nabla_r \log(Z) = 0.05$) (dex kpc ⁻¹)
01a	0.115	0.120	0.108
02	0.038	0.037	0.032
03	0.094	0.087	0.072
04a	0.049	0.044	0.035
05a	0.071	0.069	0.058
06a	-0.072	-0.068	-0.058
06b	-0.053	-0.049	-0.039
07a	0.135	0.128	0.107
07b	0.234	0.219	0.181
09	0.189	0.159	0.120
10a-E	0.023	0.021	0.018
11	0.040	0.035	0.028
13	0.077	0.079	0.070
14	0.053	0.049	0.040
15	0.062	0.064	0.058
19	0.063	0.055	0.044
20	-0.035	-0.035	-0.030
22a	-0.033	-0.028	-0.022
25	0.105	0.085	0.062
VC-7875	0.043	0.043	0.041

Notes. Similar to Table 3, but with beam-correction factors applied based on the correction curves in Fig. 9 derived in Sect. 6, for different assumed intrinsic metallicity gradients $|\nabla_r \log(Z)| = [0.20, 0.10, 0.05]$ (from left to right).

Table E.4: Literature sample of metallicity gradients and kinematics.

z	Reference (Survey)	Kinematics Reference
$0.1 < z < 3.5$	Stark et al. (2008)*	Stark et al. (2008)
	Queyrel et al. (2012) (MASSIV)	Epinat et al. (2012)
	Swinbank et al. (2012a) (SHIZELS)	Swinbank et al. (2012a)
	Jones et al. (2013)*	Jones et al. (2013)
	Stott et al. (2014) (KMOS-HiZELS) ^b	Stott et al. (2014)
	Troncoso et al. (2014) (AMAZE-LSD)	Gnerucci et al. (2011)
	(see also Cresci et al. 2010)	
	Jones et al. (2015) (GLASS-HST)*	...
	Leethochawalit et al. (2016) ^{a,*}	Leethochawalit et al. (2016)
	Wuyts et al. (2016a) (KMOS ^{3D})	Übler et al. (2019)
	Molina et al. (2017) (SHiZELS)	Molina et al. (2017)
	Wang et al. (2017) (GLASS-HST)*	Di Teodoro et al. (2018); Hirtenstein et al. (2019); Girard et al. (2020)
	(see also Yuan et al. 2011)	
	Carton et al. (2018) (MUSE-WIDE)	Sharda et al. (2021b)
	Förster Schreiber et al. (2018) (SINS/zC-SINF)	Förster Schreiber et al. (2018)
	Girard et al. (2018)*	Girard et al. (2018)
	Patrício et al. (2019)*	...
	Sharon et al. (2019)*	Liu et al. (2023)
	Wang et al. (2019) (GLASS-HST)	...
	Curti et al. (2020a) (KLEVER)*	...
	Wang et al. (2020)*	Hirtenstein et al. (2019); Girard et al. (2020)
	Gillman et al. (2021) (KROSS-KGES)	Harrison et al. (2017); Johnson et al. (2018); Tiley et al. (2021)
	Simons et al. (2021) (CLEAR)	...
	Gillman et al. (2022) (KURVS)	Puglisi et al. (2023)
	Wang et al. (2022) (GLASS-JWST)*	...
	Li et al. (2022) (MAMMOTH-Grism)	...
Barišić et al. (2025) (MSA-3D)	Barišić et al. (2025)	
Ju et al. (2025) (MSA-3D)	Ju et al. (2025)	
$z > 3.5$	Troncoso et al. (2014) (AMAZE-LSD)	Troncoso et al. (2014)
	Arribas et al. (2024) (GA-NIFS)	Arribas et al. (2024)
	Vallini et al. (2024)	Parlanti et al. (2023); Posses et al. (2023)
	Venturi et al. (2024) (JWST GO #1893 ^c)	...
	Li et al. (2025a)	...

Notes. ^(a) When available, stellar masses are taken from Mainali et al. (2023) and Wang et al. (2024), respectively. For other objects, we take the approximate median $\log(M_*/M_\odot) = 9.3$ for the entire sample. ^(b) Included the KMOS-HiZELS-SV1 sample from Sobral et al. (2013), and we adopt the kinematics results presented therein. ^(c) Carniani et al. (2021) ^(*) Gravitationally lensed.